

# Surface Properties, Orbital Dynamics, and Thermophysical Modeling of the Primitive Asteroid (269) Justitia

L. BRAGA,<sup>1</sup> A. AMARANTE,<sup>1</sup> A. FERREIRA,<sup>1</sup> F. MONTEIRO,<sup>1</sup> AND M. MARTINS<sup>1</sup>

<sup>1</sup>*São Paulo State University (UNESP), School of Engineering and Sciences, Guaratinguetá, São Paulo, Brazil*

## ABSTRACT

The Emirates Mission to the Asteroid Belt (EMA) will study the ultra-red asteroid (269) Justitia. In this work, we present the first detailed investigation of Justitia’s surface dynamics using the newly developed 3-D polyhedral shape model with 574 vertices and 1,144 faces. We analyze its geopotential, surface acceleration, escape speeds, slopes, and equilibrium points, and we also search for planar symmetric periodic orbits using an equivalent ellipsoidal approximation. Our results indicate that the lowest geopotential values occur at the poles, which also correspond to regions of maximum surface acceleration. The global slope distribution suggests preferred zones of material accumulation or migration, offering clues to Justitia’s long-term morphological evolution. Most slopes remain below 40°, implying that loose particles may settle stably across large portions of the surface. We identify five equilibrium points consistent with Justitia’s estimated density and slow rotation period. Two external points (E<sub>2</sub> and E<sub>4</sub>) exhibit linear stability, and all equilibrium locations lie relatively far from the surface due to the body’s slow spin. Additionally, we discover 28 new families of planar symmetric periodic orbits, then classify their topologies and determine their linear stability, providing a dynamical framework relevant to future spacecraft operations near Justitia. Finally, thermal modeling reveals how thermal inertia and heliocentric distance shape Justitia’s temperature distribution. The south pole receives more insolation than the north pole, reaching minimum temperatures of about 102 K and 87 K, respectively. These combined dynamical and thermal results offer valuable insights for the EMA mission and for understanding slowly rotating small bodies.

*Keywords:* Computational Methods (1965) — Main belt asteroids (2036) — Asteroid dynamics (2210) — Celestial mechanics (211)

## 1. INTRODUCTION

Primitive asteroids can transport water and complex organic molecules, which may have reached the primitive Earth through impacts, contributing to the emergence of life on the planet (Morbidegli et al. 2000; Izidoro et al. 2013). In this sense, understanding their composition, internal structures, and evolution is crucial for comprehending the formation of the Solar System. In addition, asteroids arouse the interest of the mining industry due to their potential for economic exploration (Lewis 1997). Both the mining industry and space agencies, such as NASA, ESA, and JAXA, have been investigating these celestial bodies and the changes they have undergone during the evolution of the Solar System.

In 2004, the ESA Rosetta mission (Glassmeier et al. 2007; Roll et al. 2016) captured images of the asteroids (2867) Steins and (21) Lutetia during its trajectory to comet 67P/Churyumov-Gerasimenko in 2008 and 2010, respectively. The NASA New-Horizons mission in 2015

carried out a detailed study of the dwarf planet Pluto, its moon Charon, and the small satellites Styx, Nix, Kerberos, and Hydra, as well as the Kuiper Belt Object (KBO) (486958) Arrokoth in January 2019 (Stern 2008; Stern et al. 2019). In 2014, JAXA launched the Hayabusa2 mission to collect samples from the asteroid (162173) Ryugu and return to Earth in 2020 with the samples (Hirabayashi et al. 2021). The NASA OSIRIS-REx mission, launched in September 2016, arrived at the asteroid (101955) Bennu in 2018 and returned to Earth with carbon-rich samples in September 2023. Bennu was chosen because it is a potentially hazardous asteroid. In addition, Bennu was the first asteroid to be seen ejecting particles from its surface (Lauretta et al. 2017, 2019).

In October 2021, NASA launched the Lucy mission to explore seven Trojan asteroids orbiting Jupiter, which are considered fossils from the formation of the Solar System. In November 2023, the probe arrived at the main-belt asteroid (152830) Dinkinesh, confirming that

this asteroid is a binary system (Levison et al. 2024). In April 2025, the spacecraft made a close approach to the asteroid (52246) Donaldjohanson (Marchi et al. 2025). Finally, the NASA Psyche mission, launched in October 2023, aims to investigate the asteroid (16) Psyche, which is believed to be an exposed metallic core of an unformed planet or a composition of primordial material rich in metal that has not undergone complete fusion (Elkins-Tanton et al. 2017).

In this context, several studies have explored the surface dynamics of small bodies, such as Bennu, Ryugu, Psyche, and Arrokoth, revealing key insights into their geophysical environments.

Scheeres et al. (2016) investigated the dynamic processes on the surface of the asteroid Bennu and identified slopes smaller than  $45^\circ$ , with the highest values in the intermediate areas between the equator and the poles of the northern and southern hemispheres of its surface, and lower values in the central regions along the equator. Moura et al. (2020) analyzed the gravitational field, topography, and dynamics around the asteroid Psyche in detail, revealing that it has a low-tilt surface. They also identified four external equilibrium points, of which two are stable, which could assist the mission.

Amarante & Winter (2020) explored in detail the surface dynamics of KBO Arrokoth. They identified seven equilibrium points of Arrokoth with different topological stabilities. They found that Arrokoth’s equator is an unstable region due to its high rotational period, while its polar regions are stable for surface particles. Amarante et al. (2021) used a spherical cloud of particles to determine the reaggregation density on Bennu’s surface and identified that 30% of the initial particles that are in retrograde orbits collide with its surface, proving to be more stable than the particles that are in prograde orbits, where half of the particles collided with the asteroid’s surface during the entire integration.

Fu et al. (2024) identified 25 families of bifurcated initial periodic orbits associated with Ryugu’s outer equilibrium points. The same bifurcation points connect these different bifurcated families. Furthermore, comparing Bennu and Ryugu, it is observed that in both asteroids, the bifurcation of equilibrium-point branches occurs from a degenerate point as their rotation rates increase.

Therefore, studying the surface dynamics of small bodies enables us to understand how the gravitational environment affects the surface of irregularly shaped minor bodies, which can provide important support for future missions to these small worlds of the Solar System, such as the Emirates Mission to explore the Aster-

oid Belt (EMA) (Almazmi et al. 2024; Sorli et al. 2024; Scheeres et al. 2025; El-Maarry et al. 2025).

The EMA mission will study six asteroids before reaching its final destination: the asteroid (269) Justitia, which exhibits an intensely reddish coloration due to the possible presence of organic compounds on its surface, a characteristic unusual for asteroids located in this region of the main asteroid belt. Recently, a new taxonomic type (Z-type) was introduced to classify these asteroids, which, like Justitia, exhibit very red colors and spectra and are considered ultra-red asteroids (Mahlke et al. 2022).

In this sense, the analyses and comparisons indicate that Justitia’s properties resemble Centaurs and Trans-Neptunian Objects (TNOs) (Hasegawa et al. 2021; Humes et al. 2024). Thus, it is possible that these asteroids were thrown into the main belt, as predicted by migration models of Solar System formation (Tsiganis et al. 2005; Morbidelli et al. 2005; Morbidelli 2010). Therefore, it is essential to study this class of small bodies to understand the dynamic evolution of the inner Solar System.

For example, Parker et al. (2024) presented the proximity operations strategy of the EMA mission, with an emphasis on mapping and landing on (269) Justitia using carefully planned orbits and correction maneuvers. Moreover, Marciniak et al. (2025) constrained the diameter of asteroid (269) Justitia to 55-60 km and derived its rotational period of 33.12962 h, shape, thermal inertia, and surface roughness. Buie et al. (2025) found an irregular shape for Justitia with a circular-equivalent radius of 28.5-28.9 km and a visual albedo of  $0.072 \pm 0.007$  from a multi-station occultation campaign.

Furthermore, Harish et al. (2025) analyzed the composition of the surface of the asteroid Justitia and concluded that its surface is composed of a combination of silicates altered by space weathering and carbonaceous material, which explains some of its physical characteristics, such as albedo and the features observed in the thermal infrared, which indicates that Justitia possibly underwent complex evolutionary processes, thus representing an object that formed in the region of the giant planets and later implanted into the main belt.

In this work, we provide a detailed dynamical analysis of the surface of asteroid (269) Justitia, aiming to support the EMA Mission. We explored the surface characteristics of asteroid Justitia, including the geopotential surface, surface acceleration, escape speed, and surface slope distribution. Additionally, we analyzed the number, location, and stability of equilibrium points.

We also analyze the global behavior of the slopes on Justitia’s surface, considering the third-body (3B) per-

turbation in the Main Belt and the solar radiation pressure (SRP) in both the Main Belt and the Kuiper Belt, assuming that Justitia originated in the latter region.

We investigate the evolution of the equilibrium points, assuming that Justitia’s past spin was faster than its current one, and verify how these points behave as the rotational period increases.

Furthermore, planar symmetric periodic orbits around asteroid Justitia were explored by employing an equivalent ellipsoidal approximation for its irregular shape. These periodic solutions help to understand the system’s global behavior.

Finally, we evaluate the surface temperature of Justitia under different thermal inertia values and heliocentric distances using the Thermophysical Model.

## 2. POLYHEDRON METHOD

Many numerical models have been developed to approximate the gravitational potential of irregularly shaped bodies, including asteroids. They include triaxial ellipsoids (Werner 1994), massive straight-line segments (Riaguas et al. 1999), and solid circular rings (Broucke & Elipe 2005). Methods such as Legendre polynomials also generate inaccuracies at specific points (Scheeres 1994).

A numerical approach that reduces computational effort is to model the gravitational potential of small bodies with irregular shapes using a uniform grid of point masses (mascons) that occupy the volume. Then, the total gravitational potential is obtained by summing the gravitational potential contributions of each mass (Glassmeier et al. 2007). However, this approach suffers from inaccuracies near the surface of the irregular body (Werner & Scheeres 1996). Then, more robust numerical methods are required to compute the gravitational potential near an asteroid’s surface, enabling the study of surface characteristics, such as the geopotential.

In this scenario, the polyhedron method is widely used to accurately estimate the gravitational field generated by an irregularly shaped minor body, particularly near its surface. Werner & Scheeres (1996) refined this technique by employing a harmonic expansion based on a polyhedron with constant density. They demonstrated that errors in the expressions for the gravitational potential were more significant near the surface of an asteroid than with spherical harmonics or the mascon method. Tsoulis & Petrovi (2001); Tsoulis (2012) developed a numerical approach to address these singularities by deriving specific terms to manage the computation points associated with the gravitational potential from polyhedral sources near the surface.

For this purpose, we investigate the surface characteristics of asteroid Justitia in detail, using the newly 2025 convex 3-D polyhedral shape model of asteroid Justitia consisting of 574 vertices and 1,144 faces (Marciniak et al. 2025), constructed through the lightcurve inversion method Kaasalainen & Torppa (2001); Kaasalainen et al. (2001). The 3-D polyhedral shape model of asteroid Justitia has an equivalent diameter of 59.0 km (Marciniak et al. 2025). Moreover, a rotational period of 33.12962 h was derived by Marciniak et al. (2025); Buie et al. (2025). This rotational period is consistent with those derived by Pilcher (2016).

The density of a small body is one of its essential properties and can vary considerably depending on its composition or internal structure. We applied the following bulk density ranges corresponding to the possible taxonomic classes of asteroids D-type  $1.0 \text{ g cm}^{-3}$  and analogous primitive meteorites  $\sim 1.6 - 2.3 \text{ g cm}^{-3}$  (Marchis et al. 2014; McMahon et al. 2023; Parker et al. 2024). Then, we investigate the effects of surface dynamics in a range of densities from  $1.0 \text{ g cm}^{-3}$  to  $2.0 \text{ g cm}^{-3}$ .

We adopted the MINOR-GRAVITY package<sup>2</sup> (Amarante & Winter 2020; Amarante 2020a) to compute the surface characteristics of asteroid Justitia, calculating the gravitational potential by the polyhedron method that avoids singularities over the surface of the asteroid (Tsoulis & Petrovi 2001; Tsoulis 2012), including its first and second-order derivatives (Appendix A, Eqs. (A1)-(A5)).

In addition, we also determined the number, location, and stability of equilibrium points around Justitia using the MINOR-EQUILIBRIA package<sup>3</sup> (Amarante & Winter 2020; Amarante 2020b).

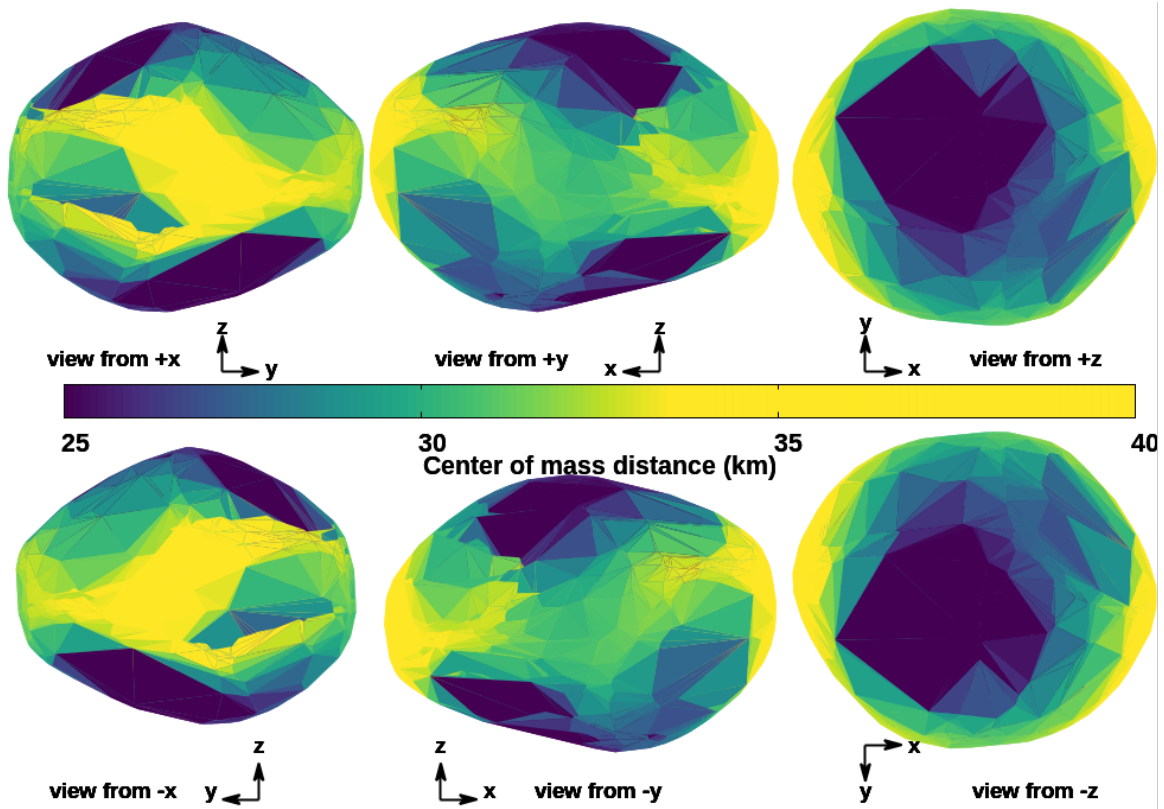
## 3. SHAPE MODEL AND GEOPOTENTIAL SURFACE

Figure 1 illustrates the 3-D polyhedral shape of asteroid Justitia, composed of 574 vertices and 1,144 faces in six perspectives:  $\pm x$ ,  $\pm y$ , and  $\pm z$ . The color box code indicates the distance between each triangular face and the asteroid’s center of mass. These distances provide complementary information for investigating the geopotential surface and surface acceleration (sec. 5).

The sum of gravitational and centrifugal potentials defines the geopotential of an asteroid. If the reference frame of the asteroid is on principal axes of inertia and centered on its barycenter, the geopotential could be

<sup>2</sup> <https://github.com/a-amarante/minor-gravity>

<sup>3</sup> <https://github.com/a-amarante/minor-equilibria-nr>



**Figure 1.** 3-D polyhedral shape model of asteroid Justitia presented in six perspective views ( $\pm x$ ,  $\pm y$ , and  $\pm z$ ). The shape model consisted of 574 vertices and 1,144 triangular faces. The color code indicates the distance from the centroid of each face to the asteroid’s center of mass, in km.

computed as (Scheeres 2012):

$$V(\mathbf{r}) = -\frac{1}{2}\omega^2 (x^2 + y^2) + U(\mathbf{r}), \quad (1)$$

where  $\mathbf{r}$  denotes the position of the particle in the reference frame attached to the asteroid about the center of mass,  $\omega$  represents the angular speed, and  $U(\mathbf{r})$  corresponds to the gravitational potential obtained numerically (Appendix A, Eq. (A1)). Fig. 2 shows the geopotential computed across the surface of asteroid Justitia for a chosen density of  $1.0 \text{ g cm}^{-3}$  and a rotational period of 33.12962 h. The views from -x, -y enhance the maximum geopotential values, while the **View from -z** represents the minimum ones.

Figures 1 and 2 show that regions far away from the center of mass have maximum values of the geopotential surface, while those close to the center of mass have low values of the geopotential surface.

Comparing the geopotential of asteroid Justitia with those found on asteroid (25143) Itokawa and KBO Arrokoth, as it is currently located in the main asteroid belt and may have similar properties to TNOs (Hasegawa et al. 2021), we have that the minimum geopotential of Justitia is  $\sim 35.5\times$  smaller than that of Itokawa (Scheeres 2012). Furthermore, it is  $\sim 4.5\times$  smaller than

**Table 1.** Global maximum and minimum geopotential, in  $\text{km}^2 \text{ s}^{-2}$ , computed over the surface of asteroid Justitia for different densities.

Density ( $\text{g cm}^{-3}$ )	Min. value ( $\times 10^{-4}$ )	Max. value ( $\times 10^{-4}$ )
1.0	-2.5	-2.0
1.2	-3.1	-2.5
1.4	-3.6	-2.9
1.6	-4.1	-3.3
1.8	-4.6	-3.7
2.0	-5.1	-4.1

that of Arrokoth (Amarante & Winter 2020). Table 1 shows that the global behavior of the geopotential distribution (Fig. 2) over the surface of Justitia does not change significantly, keeping the same order of magnitude ( $10^{-4}$ ), in the interval of densities  $1.0\text{-}2.0 \text{ g cm}^{-3}$ .

#### 4. EQUIPOTENTIAL CURVES

As the gravity field of Justitia is dominated by the gravitational potential, in Sections 4 and 6 we computed the equipotential curves and gravitational acceleration around the asteroid, respectively. Figure 3 shows the equipotential surface of Justitia and its contour lines in

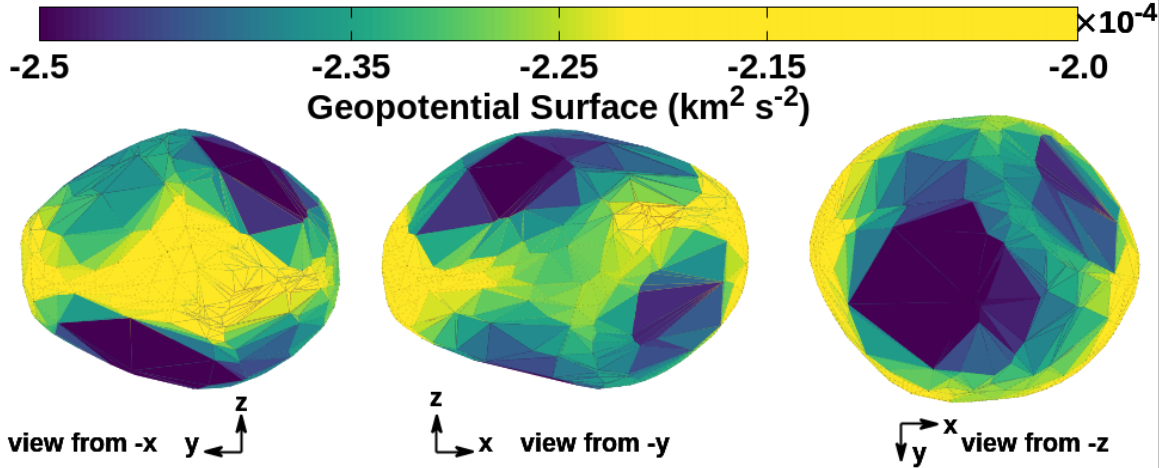


**Figure 2.** Geopotential distribution over the surface of asteroid Justitia, assuming a bulk density of  $1.0 \text{ g cm}^{-3}$  and a rotational period of 33.12962 h, shown from views  $-x$ ,  $-y$ , and  $-z$ . The color scale indicates the computed values from Eq. (1), expressed in  $\text{km}^2 \text{ s}^{-2}$ .

the  $xOy$  plane. The colors indicate the gravitational potential  $U(\mathbf{r})$ . The projection lines of asteroid Justitia are highlighted in black. Figure 3 shows that  $U(\mathbf{r})$  near the surface of Justitia ranges from, approximately,  $-2.25 \times 10^{-4} \text{ km}^2 \text{ s}^{-2}$  to  $-1.5 \times 10^{-4} \text{ km}^2 \text{ s}^{-2}$ , consistent with geopotential surface (Fig. 2). This behavior suggests that the centrifugal potential does not significantly affect Justitia’s gravity field.

## 5. SURFACE ACCELERATION

By taking the gradient of geopotential at any  $\mathbf{r}$  location on the surface of Justitia, we obtain its surface acceleration from Eq. (2):

$$\| -\nabla V(\mathbf{r}) \| . \quad (2)$$

The surface acceleration is given as the magnitude of the vector sum of the gravitational and centrifugal acceleration vectors. Figure 4 shows the surface acceleration calculated at the barycenter of each triangular face of the polyhedral model of the asteroid Justitia. Figures 2 and 4 show that the regions of maximum surface acceleration View from  $-z$  correspond to the regions of minimum surface geopotential View from  $-z$ . In contrast, the regions of minimum surface acceleration correspond to the regions of maximum geopotential (views from  $-x$ ,  $-y$ ). This phenomenon occurs because the ratio between the order of magnitude of gravity and the potential of the centrifugal force is  $\sim 100$  ( $\mathcal{K}$  parameter from Eq.(13)).

## 6. GRAVITATIONAL ACCELERATION

Figure 5 shows the distribution of the magnitude of the gravitational acceleration vector around asteroid Justitia. The contour lines are visualized through projections:  $xOy$ ,  $xOz$ , and  $yOz$ , with color mapping indicating the magnitude of the gravitational acceleration

**Table 2.** Global maximum and minimum surface acceleration, in  $\text{km s}^{-2}$ , computed over the surface of asteroid Justitia for different densities.

Density ( $\text{g cm}^{-3}$ )	Min. value ( $\times 10^{-6}$ )	Max. value ( $\times 10^{-6}$ )
1.0	7.5	8.5
1.2	8.6	9.8
1.4	10.1	11.5
1.6	11.5	13.1
1.8	13.0	15.0
2.0	14.5	16.4

vector  $\| -\nabla U(\mathbf{r}) \|$ . We observe that the gravitational acceleration at the surface of asteroid Justitia is stronger than in regions near its center of mass, due to its mass distribution. The higher values of gravitational acceleration are found near the asteroid’s surface. They can reach values of  $\sim 8 \times 10^{-6} \text{ km s}^{-2}$ , similar to those found for the surface acceleration (Fig. 4). Comparing the surface acceleration of Justitia with those found in the asteroids Bennu and Psyche, we have that the minimum acceleration of Justitia is  $\sim 310\times$  larger than that of Bennu (Scheeres et al. 2016) and  $\sim 18\times$  smaller than that of Psyche (Moura et al. 2020).

Table 2 shows the global behavior of the results for the surface acceleration of asteroid Justitia for different densities. We observe that if the density is doubled, the surface acceleration approximately doubles.

## 7. SURFACE SLOPES

Considering a location  $\mathbf{r}$  on the surface of Justitia, the relative orientation between the normal unit vector to this surface  $\hat{\mathbf{n}}$  and the gradient of geopotential calculated at point  $\mathbf{r}$  will establish the surface slope (Scheeres et al.

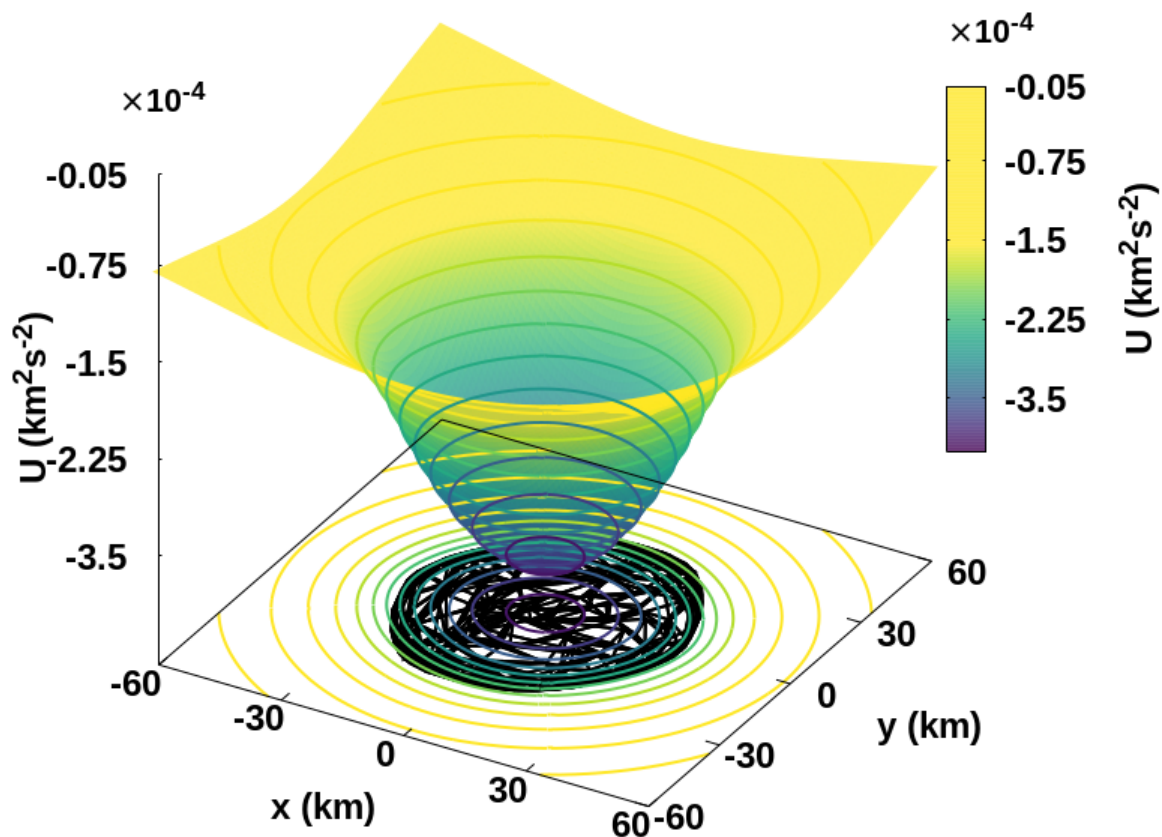


**Figure 3.** Equipotential surface of Justitia and its contour lines in the  $xOy$  plane. The color box denotes the gravitational potential,  $U(\mathbf{r})$ , in  $\text{km}^2 \text{s}^{-2}$  around Justitia (black).

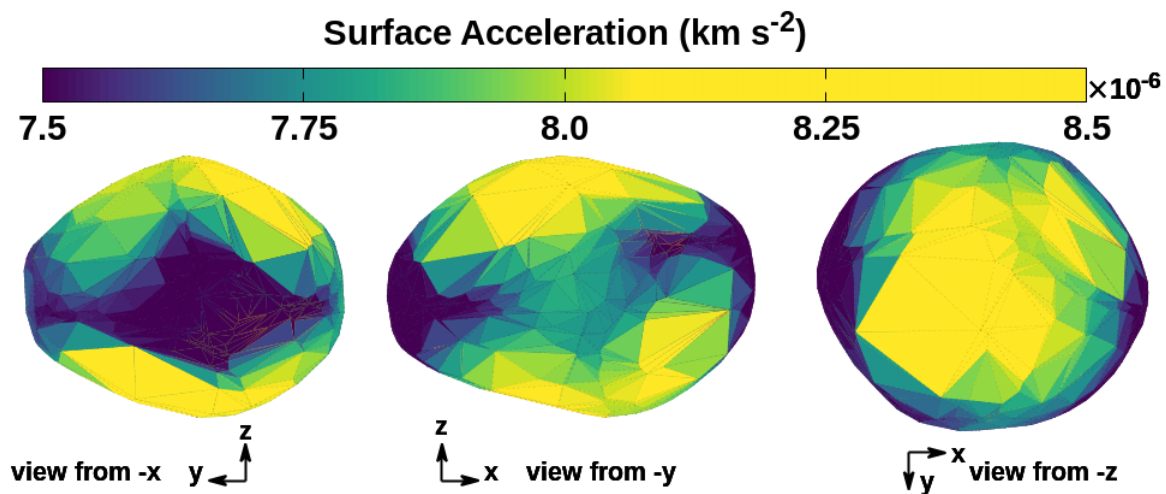


**Figure 4.** The surface acceleration distribution across asteroid Justitia is presented from three orthogonal perspectives ( $-x$ ,  $-y$ , and  $-z$ ). The color bar represents the magnitude of the vector sum of the gravitational and centrifugal acceleration vectors  $\|\nabla V(\mathbf{r})\|$  at the barycenter of the facet, in  $\text{km s}^{-2}$ .

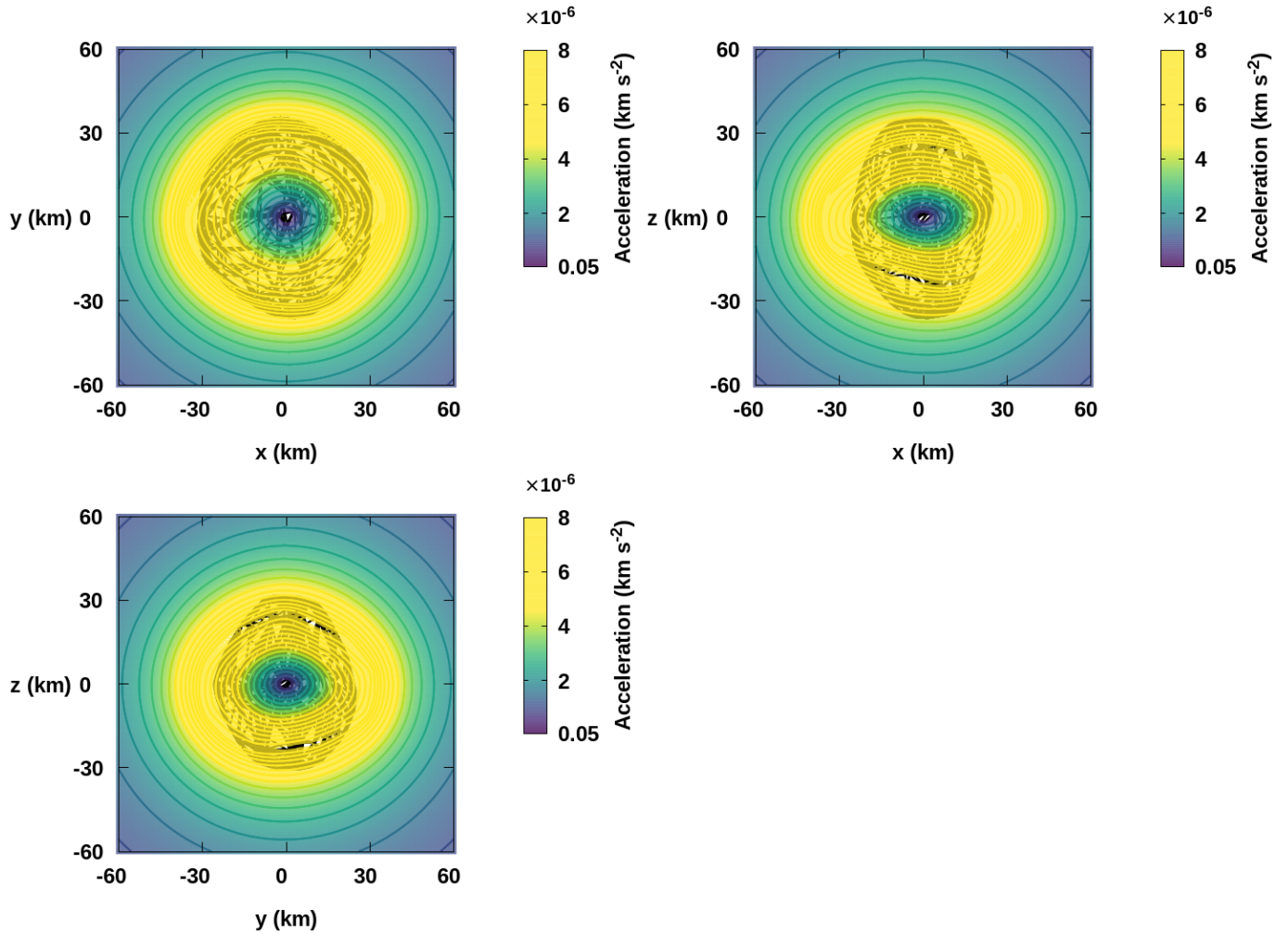


**Figure 5.** Gravitational acceleration around and inside Justitia in three orthogonal projections:  $xOy$ ,  $xOz$ , and  $yOz$  planes. The contour lines represent lines of force. The color bar indicates the magnitude of the gravitational acceleration vector  $\| -\nabla U(\mathbf{r}) \|^2$ , measured in  $\text{km s}^{-2}$ .

2016). The slope  $\theta$  is defined as the supplement of the angle formed by the normal vector to the surface and the surface acceleration vector at point  $\mathbf{r}$  (see eq. (3)). This dynamic characteristic provides insight into the motion of particles on the surface of the asteroid Justitia. If  $\theta > 90^\circ$ , the particles are possibly being ejected from the asteroid's surface, while if  $\theta < 90^\circ$ , the particles may accumulate in some regions of the asteroid's surface.

$$\theta = 180^\circ - \arccos\left(\frac{-\nabla V(\mathbf{r}) \cdot \hat{\mathbf{n}}}{\|\nabla V(\mathbf{r})\|}\right) \frac{180^\circ}{\pi}. \quad (3)$$

The analysis of the slopes of Justitia shows that they do not exceed  $40^\circ$  (see Fig. 6). The distribution of maximum slopes reaches values around  $40^\circ$ , and the minimum slopes values close to  $0^\circ$ . Our results show that 97.5% of the surface of asteroid Justitia has slopes below  $30^\circ$ .

Some bodies with surface slopes less than  $30^\circ$ , such as Beta and Gamma of the triple asteroid system (153591) 2001 SN<sub>263</sub> (Winter et al. 2020) and (16) Psyche (Moura et al. 2020), suggest that globally there is a low possibility of ejecting particles (Scheeres 2012).

### 7.1. Disturbed Slopes

In these sections, we analyze how other perturbing forces influence the slopes on Justitia's surface, for a bulk density of  $1.0 \text{ g cm}^{-3}$ . These are the solar radiation pressure (SRP), where we assume Justitia is located in the main belt (aphelion and perihelion) and that the asteroid was previously in the Kuiper belt at  $\sim 40 \text{ au}$ . We also include the perturbation of a third body, Mars and Jupiter, respectively, due to Justitia's location in the central part of the main belt. We emphasize that, even considering different values of our density range for the asteroid Justitia, the overall behavior of the surface perturbations does not change significantly.

### 7.2. Solar Radiation Pressure Perturbation

For the SRP analysis, we consider this perturbation in a particle located at the centroid of each triangular plate of the polyhedral model. The equation of motion under the influence of SRP is given by Eq. (4) (Burns et al. 1979; Mignard 1984; Amarante et al. 2021).

$$\mathbf{a}_{\text{SRP}}(\mathbf{r}) = -\frac{Q_{\text{pr}} S_0 R_0^2}{c \|\mathbf{r}_s - \mathbf{r}\|^3} \frac{A}{m} (\mathbf{r}_s - \mathbf{r}), \quad (4)$$

where  $\mathbf{r}_s$  is the position vector of the Sun relative to Justitia,  $\|\mathbf{r}_s - \mathbf{r}\|$  is the distance from the particle's located at the barycenter of each face to the Sun,  $S_0$  is a solar constant or radiation flux density at the distance of the astronomical unit  $R_0$  (au),  $c$  is the speed of light, and  $Q_{\text{pr}}$  is the dimensionless efficiency factor for radiation pressure, which depends on the properties (e.g.,

**Table 3.** The Solar Radiation Pressure parameters used in the mathematical model.

Parameter	Value	Units
$Q_{\text{pr}}$	1	--
$S_0$	$1.36 \times 10^3$	$\text{kg s}^{-3}$
$R_0$	$1.495978707 \times 10^8$	km
$c$	$2.99792 \times 10^5$	$\text{km s}^{-1}$
$\rho$	1.0	$\text{g cm}^{-3}$
$r_{\text{pe}}$	$1 - 10^{-1}$	$\mu\text{m}$
$r_{\text{ap}}$	$3.0 \times 10^{-1} - 9.0 \times 10^{-2}$	$\mu\text{m}$
$r_{\text{Kb}}$	$5.0 \times 10^{-3} - 5.0 \times 10^{-4}$	$\mu\text{m}$

density, shape, size) of the particle. In the mathematical model, this value is assumed to be 1 to represent the value of an ideal material. The adopted SRP parameters are presented in Tab. 3.

Our objective was to determine the acceleration vector caused by solar radiation pressure (SRP) on a particle at the centroid of each face of the convex polyhedron and then add to this vector the total acceleration vector calculated in section 7. After this, we obtain the new total acceleration vector due to SRP, given by Eq. (5).

$$\mathbf{a}_{\text{total}} = \mathbf{a}_{\text{SRP}}(\mathbf{r}) - \nabla V(\mathbf{r}). \quad (5)$$

Thus, our analyses show the global behavior of the slopes, varying the particle's radius at the perihelion and aphelion of its orbit in the main belt and also varying the particle's radius in the Kuiper belt, assuming that Justitia may have originated there in the past.

Figures 7, 8, and 9, we fix the pericenter of the asteroid Justitia's orbit, and we vary the particle sizes from  $1 \mu\text{m}$  to  $10^{-1} \mu\text{m}$ , at the centroid of each face of the convex model. We find that particles  $< \sim 4 \times 10^{-1} \mu\text{m}$  on the surface of asteroid Justitia are significantly influenced by the SRP at the pericenter of the asteroid's orbit, while particles on the order of  $1 \mu\text{m}$  are not significantly influenced by the SRP.

Figures 10, 11, and 12, we fix the apocenter of the asteroid Justitia's orbit, and we vary the particle sizes from  $3 \times 10^{-1} \mu\text{m}$  to  $9.0 \times 10^{-2} \mu\text{m}$ , at the centroid of each face of the convex model. We find that particles  $< \sim 1.5 \times 10^{-1} \mu\text{m}$  on the surface of asteroid Justitia are significantly influenced by the SRP at the apocenter of the asteroid's orbit, while particles  $> 3.0 \times 10^{-1} \mu\text{m}$  are not significantly influenced by the SRP. For comparison purposes, the solar radiation pressure does not significantly affect particles across the surface of comet 67P with sizes  $\sim > 10^{-3} \text{ cm}$  at apocenter and  $\sim > 10^{-1} \text{ cm}$  at pericenter (Braga et al. 2025).

Figures 13, 14, and 15, we set Justitia at 40 au and vary the particle sizes from  $5.0 \times 10^{-3} \mu\text{m}$  to  $5.0 \times$

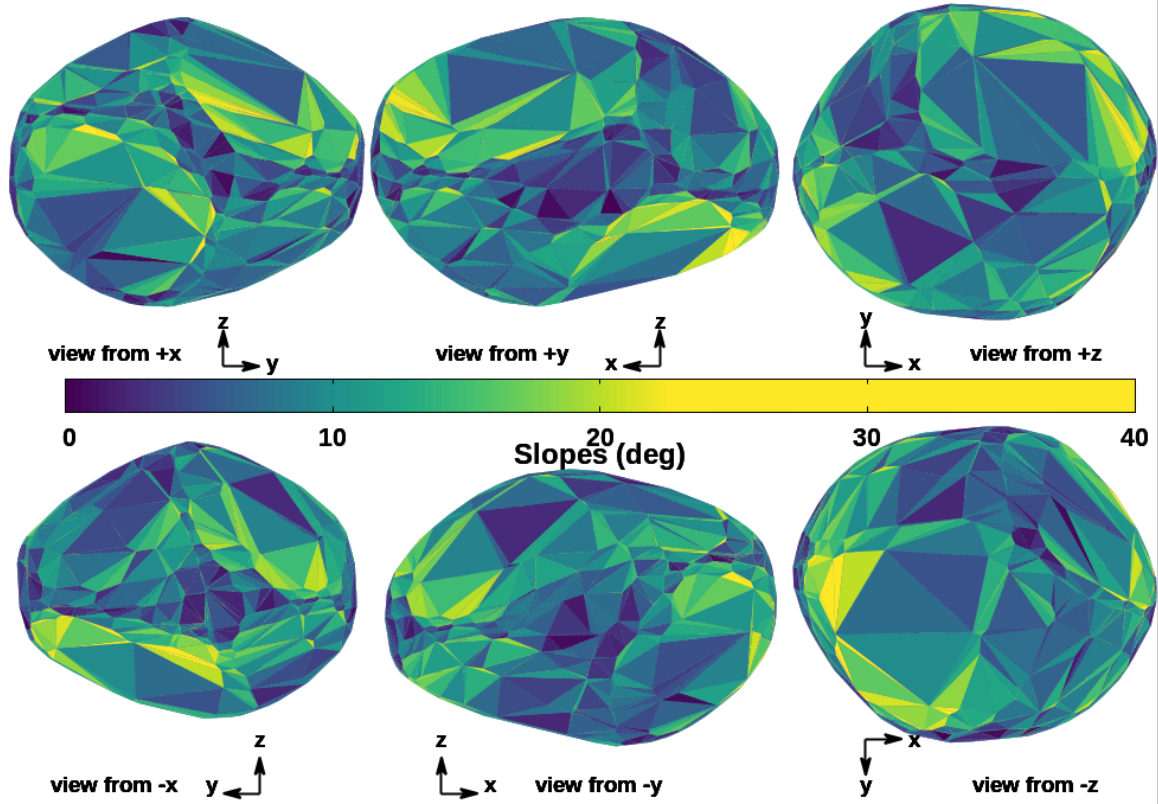


**Figure 6.** Surface slopes mapped across the surface of Justitia are viewed in six perspectives ( $\pm x$ ,  $\pm y$ , and  $\pm z$ ). The color bar indicates the slope  $\theta$  (degrees) computed numerically from Eq. (3).

$10^{-4} \mu m$ . We identified that particles  $< \sim 1.0 \times 10^{-3} \mu m$  are significantly influenced by SRP, while particles  $> 5.0 \times 10^{-3} \mu m$  are not significantly influenced by SRP. However, for this case, it is important to emphasize that other electromagnetic forces influence particles smaller than  $10^{-2} \mu m$  around irregular bodies, causing the gravitational field to become a disturbance (Mignard 1982; Horányi 1996; Amarante & Winter 2022). In this work, we do not consider these forces.

### 7.3. The disturbing effects of a Third-Body

We analyze the slopes on the surface of Justitia, considering the gravitational perturbations of Mars and Jupiter (Mars ( $M_a$ ), Jupiter (J)) on a particle located at the centroid of each face of the 3-D shape model, using Eq.(6):

$$\mathbf{a}_{\text{pert}}(\mathbf{r}) = GM_{M_a/J} \left( \frac{\mathbf{r}_{M_a/J} - \mathbf{r}}{\|\mathbf{r}_{M_a/J} - \mathbf{r}\|^3} - \frac{\mathbf{r}_{M_a/J}}{\|\mathbf{r}_{M_a/J}\|^3} \right) \quad (6)$$

where  $M_{M_a} = 6.4 \times 10^{23} \text{ kg}$  is the total mass of Mars,  $M_J = 1.9 \times 10^{27} \text{ kg}$  is the total mass of Jupiter,  $\mathbf{r}_{M_a}$  is the position vector of Mars concerning Justitia,  $\mathbf{r}_J$  is the position vector of Jupiter concerning Justitia,  $\|\mathbf{r}_{M_a} - \mathbf{r}\|$  is the distance from the barycenter vector of each face to

Mars, and  $\|\mathbf{r}_J - \mathbf{r}\|$  is the distance from the barycenter vector of each face to Jupiter.

The new slopes are now computed from Eq. (7):

$$\theta = \frac{180^\circ}{\pi} \left[ 1 - \arccos \left( \frac{-\mathbf{a}_{\text{total}}(\mathbf{r}) \cdot \hat{\mathbf{n}}}{\|\mathbf{a}_{\text{total}}(\mathbf{r})\|} \right) \right], \quad (7)$$

where  $\mathbf{a}_{\text{total}} = \mathbf{a}_{\text{pert}}(\mathbf{r}) - \nabla V(\mathbf{r})$ , and  $\hat{\mathbf{n}}$  is the normal vector calculated at the centroid of each face.

Figures 16, 17 show the behavior of the slopes due to perturbations from Mars and Jupiter, respectively. As we can see, the two bodies do not significantly affect the surface slopes of Justitia.

## 8. SURFACE TILT

Let  $\mathbf{r}$  be an arbitrary point on the surface of Justitia. The orientation of the surface at this point, in the reference frame fixed to the asteroid, is determined by the direction of the normal unit vector  $\hat{\mathbf{n}}$ . We adopt as the reference direction the vector that originates at the center of mass of the asteroid and points to the arbitrary location  $\mathbf{r}$  on its surface. Then, the angle between the normal vector  $\hat{\mathbf{n}}$  to the surface and the barycenter vector  $\mathbf{r}$  is specified as tilt (Scheeres et al. 2016).

Figure 18 shows the tilt distribution across the surface of asteroid Justitia. We observe that the variation of the

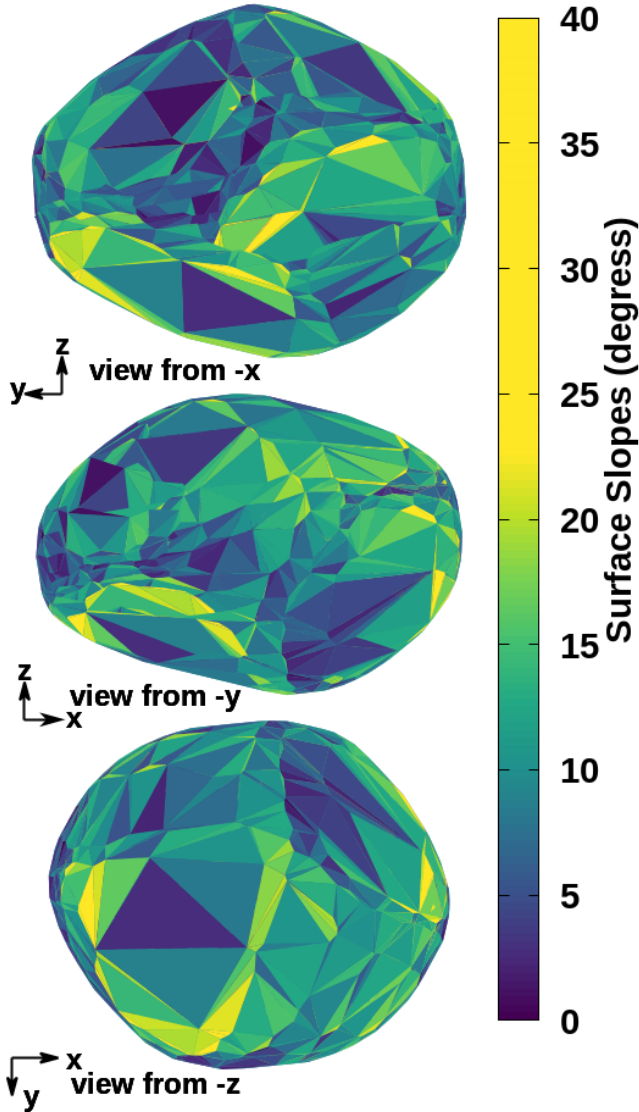


**Figure 7.** Global behavior of the slopes as a function of particle size of  $1 \mu m$ , at approximately 2.06 au. The color scale shows slopes from  $0^\circ$  to  $40^\circ$

tilt does not exceed  $50^\circ$ . The maximum values for tilt are found around  $50^\circ$ , while the minimum values are found at approximately  $0^\circ$ .

Furthermore, this entirely geometric quantity can guide the landing of a spacecraft if it wishes to reach the object's surface at a  $90^\circ$  angle. Since the tilt is an entirely geometric quantity, it will be the same regardless of the density value.

## 9. ESCAPE SPEED

The escape speed over the surface of asteroid Justitia can be calculated by combining its angular speed, surface orientation, and gravitational potential. Equation

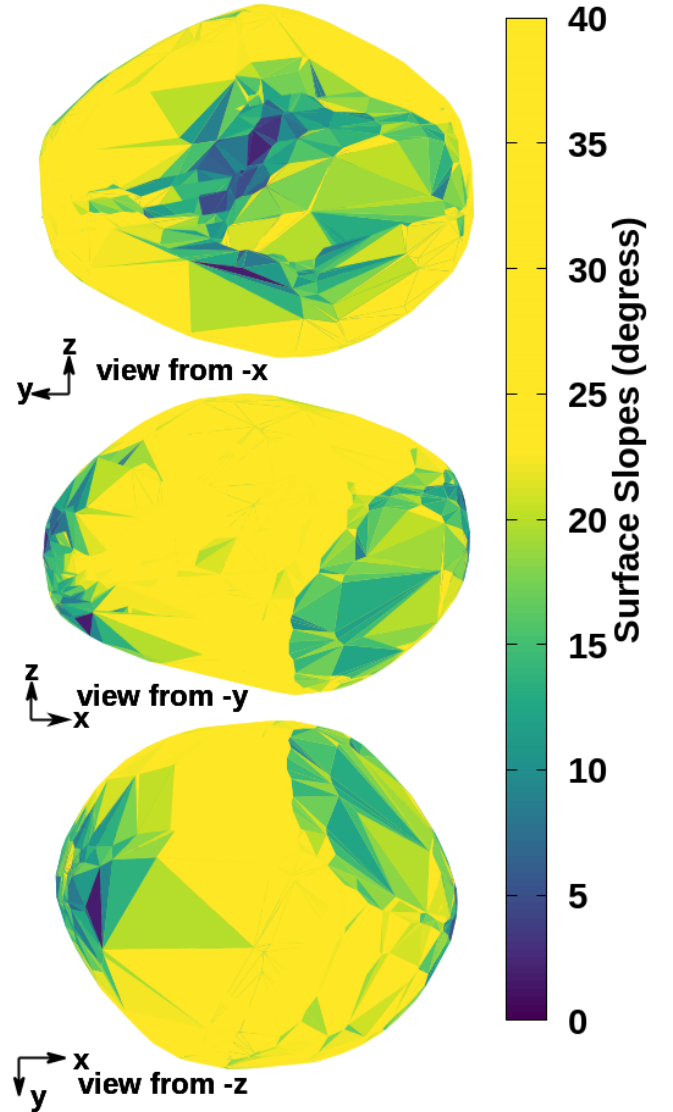


**Figure 8.** Global behavior of the slopes as a function of particle size of  $4.0 \times 10^{-1} \mu m$ , at approximately 2.06 au. The color scale shows slopes from  $0^\circ$  to  $40^\circ$

(8) gives the escape speed  $v_e$  (Scheeres et al. 2016).

$$v_e = -\hat{\mathbf{n}} \cdot (\boldsymbol{\omega} \times \mathbf{r}) + \sqrt{[\hat{\mathbf{n}} \cdot (\boldsymbol{\omega} \times \mathbf{r})]^2 - 2U_{\min} - \|\boldsymbol{\omega} \times \mathbf{r}\|^2}, \quad (8)$$

where  $\mathbf{r}$  is the radius vector from the asteroid's center of mass to the local surface,  $U_{\min} = \min \left[ U, -\frac{GM}{|\mathbf{r}|} \right]$ ,  $G = 6.67430 \times 10^{-20} \text{ km}^3 \text{ kg}^{-1} \text{ s}^{-2}$  is the gravitational constant,  $M = 1.02 \times 10^{17} \text{ kg}$  is the mass of the Justitia for a density of  $1.0 \text{ g cm}^{-3}$ ,  $\boldsymbol{\omega}$  is the angular velocity vector and  $\hat{\mathbf{n}}$  is the normal unit vector.

If the particle's speed launched exceeds the escape speed of asteroid Justitia, the particle will escape. We assume that the particle is launched in the direction nor-

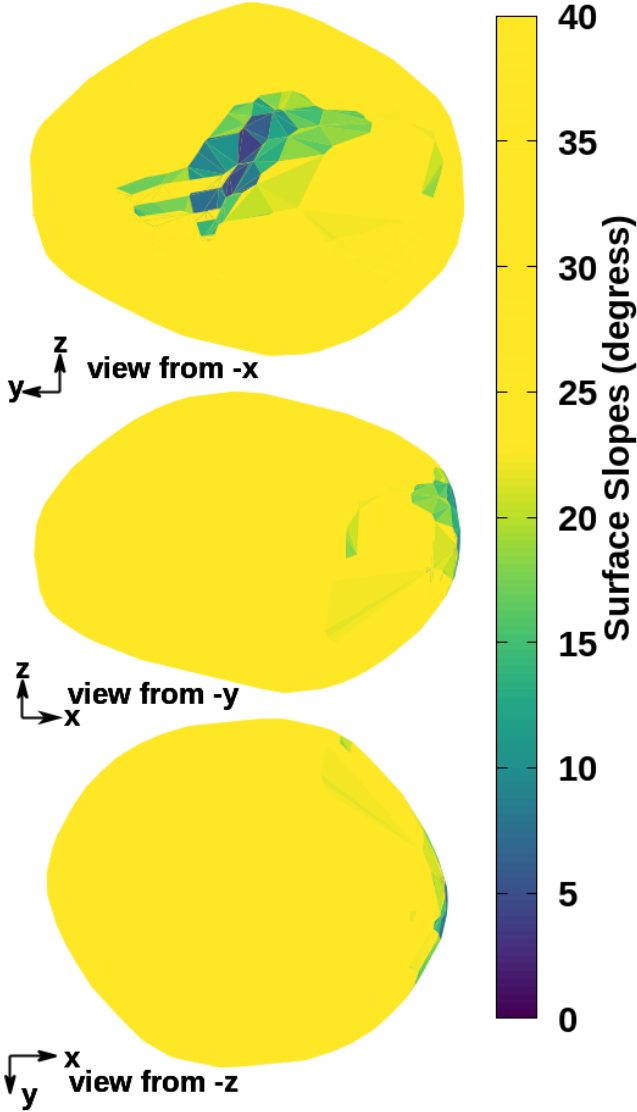


**Figure 9.** Global behavior of the slopes as a function of particle size of  $10^{-1} \mu m$ , at approximately 2.06 au. The color scale shows slopes from  $0^\circ$  to  $40^\circ$

mal to the local triangular facet of the asteroid. Fig. 19 shows the results of escape speed mapped across the surface of the asteroid Justitia.

Comparing Fig. 19 and Fig. 2, the regions of maximum escape speed correspond to the regions with minimum geopotential. This global behavior of escape speed also appears in other slowly rotating minor bodies, such as (4179) Toutatis (Scheeres et al. 1998) and KBO Arrokoth (Amarante & Winter 2020).

## 10. EQUILIBRIUM POINTS

In this section, we numerically computed the external and inner equilibrium points of the asteroid Justitia

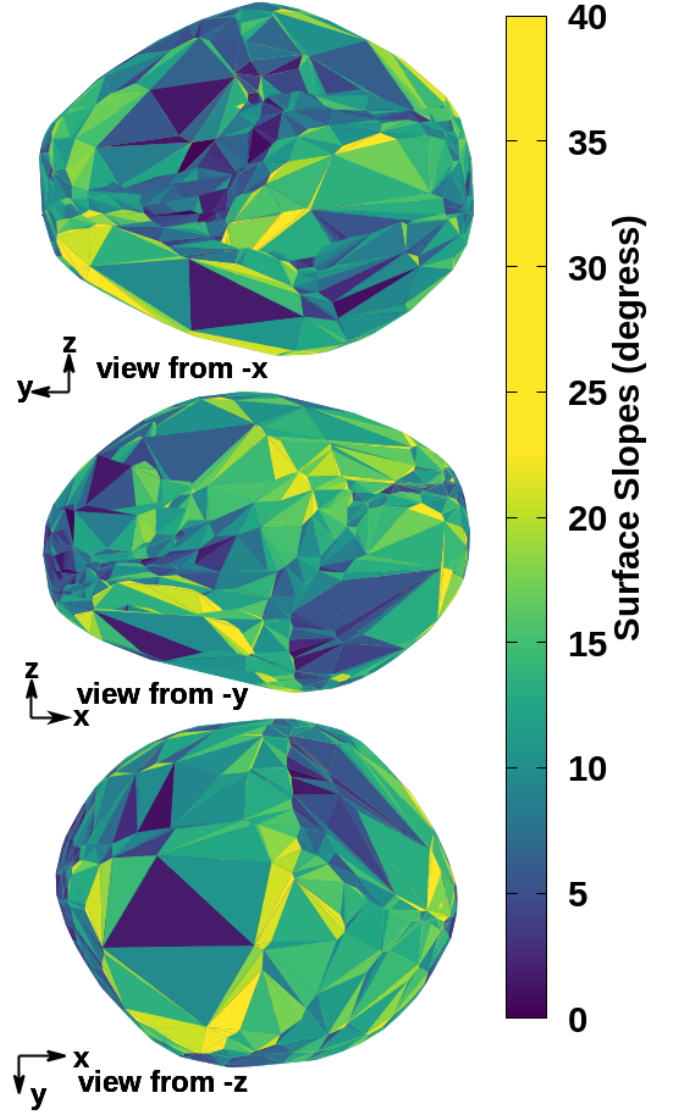


**Figure 10.** Global behavior of the slopes as a function of particle size of  $3.0 \times 10^{-1} \mu m$ , at approximately 3.17 au. The color scale shows slopes from  $0^\circ$  to  $40^\circ$ .

using the following Eq. (9).

$$\nabla V(\mathbf{r}) = 0. \quad (9)$$

We found five equilibrium points for the rotational period of 33.12962 h and a density of  $1 \text{ g cm}^{-3}$  for Justitia (Fig. 20). Two of them are unstable ( $E_1, E_3$ ) and three are linearly stable ( $E_2, E_4, E_5$ ), where  $E_5$  is located internally to the asteroid. In Table 4, we show the locations of the equilibrium points around Justitia for different density values. We observe that as the density increases, the gravitational attraction becomes stronger, while the centrifugal force remains unchanged. As a result, the equilibrium points shift outward, seeking positions where the centrifugal force balances the increased

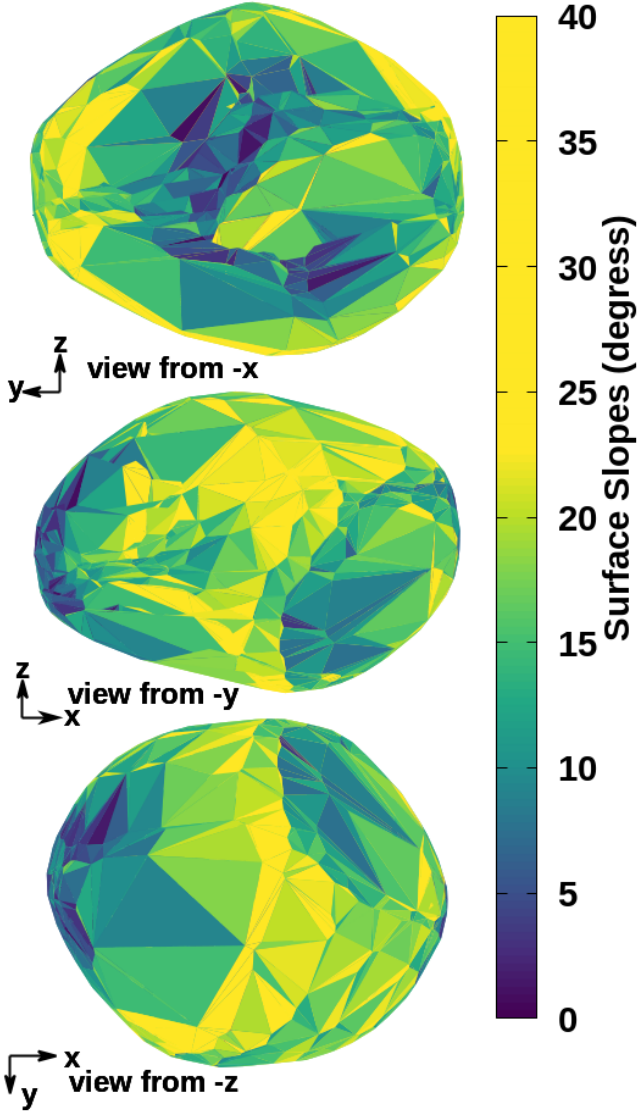


**Figure 11.** Global behavior of the slopes as a function of particle size of  $1.5 \times 10^{-1} \mu m$ , at approximately 3.17 au. The color scale shows slopes from  $0^\circ$  to  $40^\circ$ .

gravitational pull. It is interesting to note that the internal equilibrium point  $E_5$  shifts inward as the density increases.

Equilibrium points are also classified by stability. To analyze these stabilities, we applied a linearization method using the eigenvalues of the characteristic equation, as described in cases by Jiang (2015). We defined these classifications as follows: equilibrium points  $E_2$ ,  $E_4$ , and  $E_5$  have three pairs of imaginary eigenvalues, meaning they are classified as Case 1 (linearly stable). On the other hand, the equilibrium points  $E_1$  and  $E_3$  are classified as Case 2, as they present two pairs of imaginary eigenvalues (unstable).

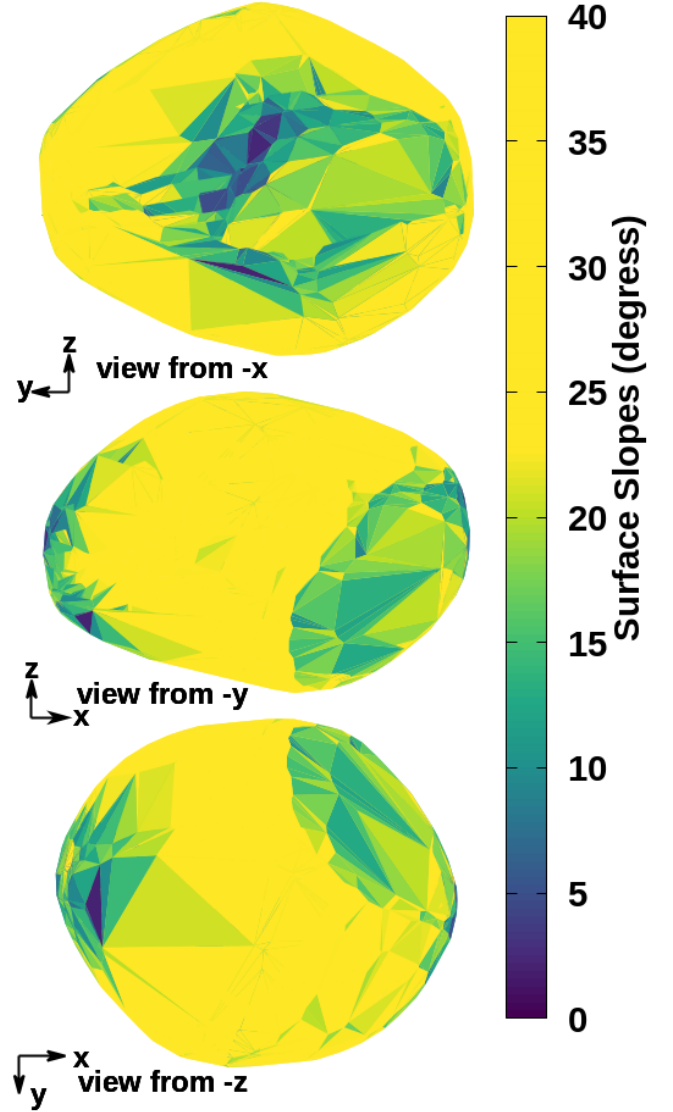


**Figure 12.** Global behavior of the slopes as a function of particle size of  $9.0 \times 10^{-2} \mu m$ , at approximately 3.17 au. The color scale shows slopes from  $0^\circ$  to  $40^\circ$ .

Table 9 (see Appendix B) gives the eigenvalues for each equilibrium point about Justitia, considering different density values. Additionally, we have assigned these topological classifications, which remain unchanged as the density increases. Based on these eigenvalues,  $E_1$  and  $E_3$  have a saddle-center-center configuration, characterizing hyperbolic instability, while  $E_2$ ,  $E_4$ , and  $E_5$  follow a center-center-center structure, being linearly stable. Thus, the asteroid Justitia can be characterized based on the distribution of its external equilibrium points as an asteroid of type I (Scheeres 1994).

**Table 4.** Location of equilibrium points around Justitia. Equilibria are computed numerically through MINOR-EQUILIBRIA package (Amarante & Winter 2020), considering the polyhedron method and an accuracy of  $10^{-5}$  for the Newton-Raphson method, assuming different densities for Justitia and a rotational period of 33.12962 h.

Equilibrium Point	Density ( $\text{g cm}^{-3}$ )	$x$ (km)	$y$ (km)	$z$ (km)
E <sub>1</sub>	1.0	135.56449	3.06619	0.01870
	1.2	143.98391	2.96037	0.01621
	1.4	151.51594	2.87370	0.01435
	1.6	158.36302	2.80081	0.01292
	1.8	164.66247	2.73825	0.01177
	2.0	170.51225	2.68369	0.01083
E <sub>2</sub>	1.0	1.49254	135.03974	-0.03475
	1.2	1.38354	143.48737	-0.03060
	1.4	1.29792	151.04212	-0.02749
	1.6	1.22820	157.90809	-0.02506
	1.8	1.16991	164.22363	-0.02311
	2.0	1.12013	170.08734	-0.02150
E <sub>3</sub>	1.0	-135.62925	-1.05365	-0.00842
	1.2	-144.04152	-0.94723	-0.00646
	1.4	-151.56810	-0.86034	-0.00511
	1.6	-158.41086	-0.78740	-0.00414
	1.8	-164.70680	-0.72490	-0.00341
	2.0	-170.55364	-0.67045	-0.00285
E <sub>4</sub>	1.0	-1.68310	-135.01066	-0.03519
	1.2	-1.58656	-143.46152	-0.03098
	1.4	-1.51020	-151.01873	-0.02783
	1.6	-1.44766	-157.88665	-0.02537
	1.8	-1.39512	-164.20377	-0.02339
	2.0	-1.35007	-170.06881	-0.02175
E <sub>5</sub>	1.0	0.13756	-0.14938	0.05430
	1.2	0.13728	-0.14911	0.05431
	1.4	0.13707	-0.14892	0.05431
	1.6	0.13692	-0.14878	0.05432
	1.8	0.13680	-0.14867	0.05432
	2.0	0.13671	-0.14858	0.05432

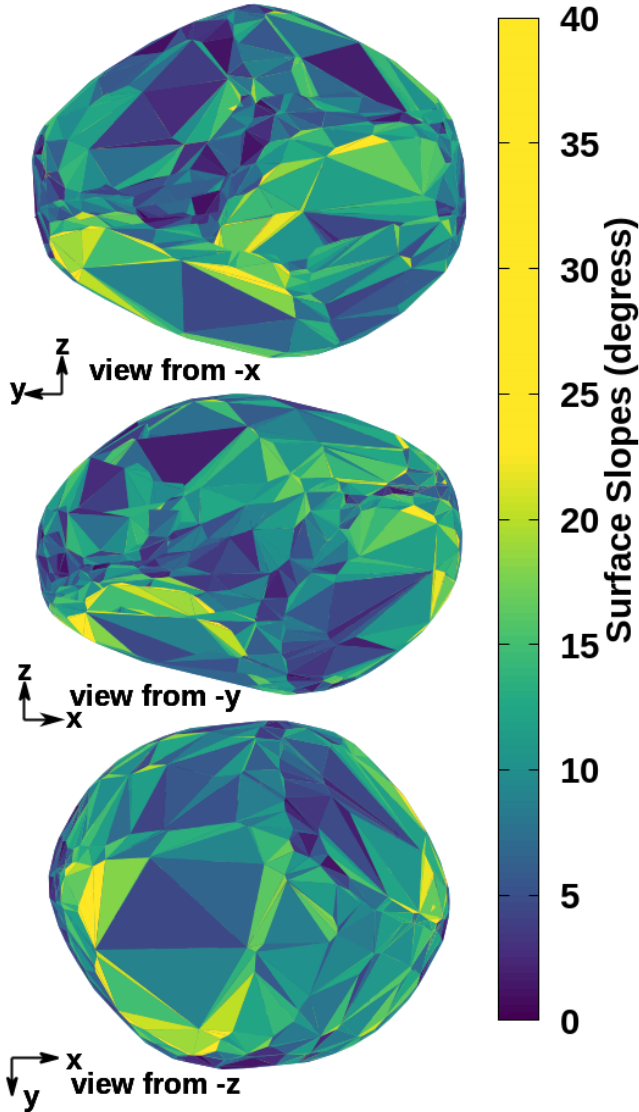


**Figure 13.** Global behavior of the slopes as a function of particle size of  $5.0 \times 10^{-3} \mu\text{m}$ , at approximately 40 au. The color scale shows slopes from  $0^\circ$  to  $40^\circ$

### 10.1. Evolution of the Equilibrium Points

In this section, we propose that Justitia may have had a faster spin in the past. From this, we analyze the evolution of the equilibrium points around Justitia for different rotational periods.

Fig. 21 illustrates the locations of the different equilibrium points calculated around Justitia. As we can see, as we decrease the rotational period of 33 hours, the equilibrium points move closer to the surface of the body, a common characteristic of slowly rotating bodies, as explained in the previous section on density variation. In other words, as we decrease the rotational period, the centrifugal force increases. For the balance

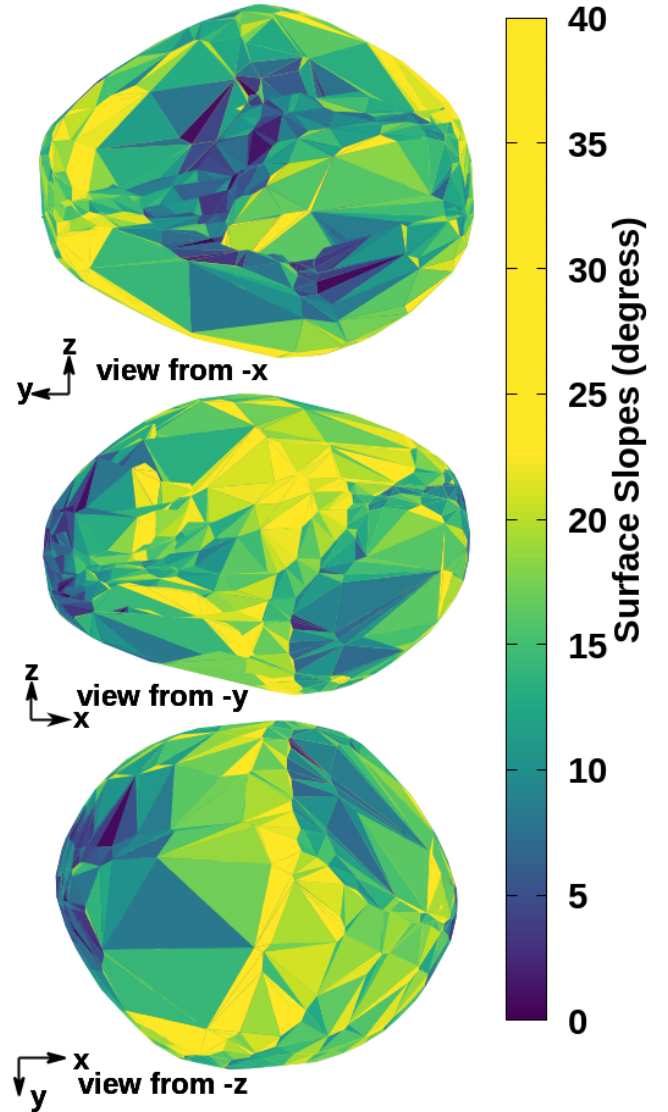


**Figure 14.** Global behavior of the slopes as a function of particle size of  $1.0 \times 10^{-3} \mu\text{m}$ , at approximately 40 au. The color scale shows slopes from  $0^\circ$  to  $40^\circ$

between gravity and this force to be limited, the equilibrium point needs to be closer to the body's surface, where the gravitational force is stronger.

## 11. ZERO-VELOCITY CURVES

Zero-velocity curves divide space into regions of allowed and not allowed motion. In general, they are any surfaces that ensure that a particle is trapped or limited by the surface of the ellipsoid (Scheeres 1994). The dynamical equations governing particle motion in the vicinity of Justitia, assuming uniform rotation about its  $z$ -axis, can be expressed as Jiang & Baoyin (2014):

$$\ddot{x} - 2\omega\dot{y} + \frac{\partial V}{\partial x} = 0, \quad \ddot{y} + 2\omega\dot{x} + \frac{\partial V}{\partial y} = 0, \quad \ddot{z} + \frac{\partial V}{\partial z} = 0. \quad (10)$$

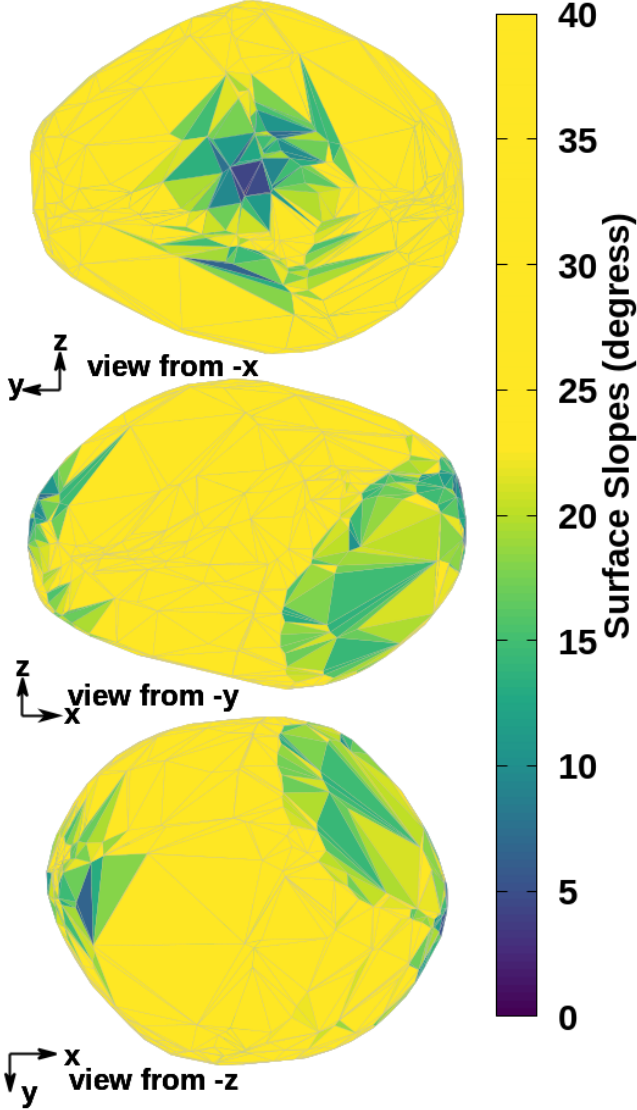


**Figure 15.** Global behavior of the slopes as a function of particle size of  $5.0 \times 10^{-4} \mu\text{m}$ , at approximately 40 au. The color scale shows slopes from  $0^\circ$  to  $40^\circ$

It is important to emphasize that these equations are related to the return speed, following the inequality:

$$J - V(r) \geq 0. \quad (11)$$

Thus, based on the value of the Jacobi constant  $J$ , the space around the asteroid can be divided into regions where the particle's movement is allowed or prohibited, reducing areas where its trajectory will be confined. Once this inequality is violated, there will be regions where movement is prohibited. Consequently, when  $V(\mathbf{r}) = J$ , the limits of these regions are called the zero-velocity curves (Murray & Dermott 1999).

Figure 22 presents the geopotential  $V(\mathbf{r}) = J$  distribution of Justitia across three projection planes: xOy,

xOz, and yOz planes, with contour lines representing constant values of the Jacobi integral. The topological structure of the equilibrium points can be determined by examining zero-velocity curves in these projection planes. The topological structure of the xOy plane confirms the existence of five equilibrium points about the asteroid Justitia. The equilibrium points  $E_1$  and  $E_3$  in projection planes xOy and xOz exhibit saddle-type geometries (unstable). In contrast, equilibrium points  $E_2$  and  $E_4$  display central-type characteristics (linearly stable) in the xOy plane. However, they present saddle-type geometries in the yOz plane. Additionally, equilibrium point  $E_5$  is a central-type point in the three projection planes.

## 12. RETURN SPEED

The curve that encompasses the asteroid Justitia and intersects at the equilibrium point with minimum Jacobi constant value  $J'$  defines the return speed  $v_r$  as Eq. (12) (Scheeres 2012):

$$v_r = \sqrt{2(J' - V(\mathbf{r}))}, \quad (12)$$

where  $V(\mathbf{r})$  represents the geopotential at location  $\mathbf{r}$ .]

The necessary condition for a particle to escape from Justitia's surface is called its return speed. However, this condition is necessary but not sufficient; in other words, if the particle has a speed greater than the return speed, it will not immediately return to the surface, but may enter a temporary orbit around the asteroid and eventually escape.

The Fig 23 shows the mapping of the return speed on the surface of Justitia, considering the bulk density of  $1.0 \text{ g cm}^{-3}$ . The value of  $J'$  used is  $7.60 \times 10^{-5} \text{ km}^2 \text{ s}^{-2}$  and is associated with the equilibrium point  $E_3$ . Note that the minimum values of the return speed (views from -x, -y) are located in the regions of minimum escape speed (Fig. 19). In contrast, the maximum values (View from -z) are distributed over the regions associated with maximum values of escape speed across the surface of asteroid Justitia.

However, these characteristics describe physically distinct phenomena. While escape speed represents the minimum speed a particle must have to completely overcome the body's gravitational field and move away from it, the return speed corresponds to the highest initial speed a particle can have when launched from the surface of Justitia and remain gravitationally bound to the body before returning to its surface.

## 13. ORBITS AROUND ASTEROID (269) JUSTITIA

The analysis of the orbital dynamics around the asteroid Justitia was conducted based on a simplified model

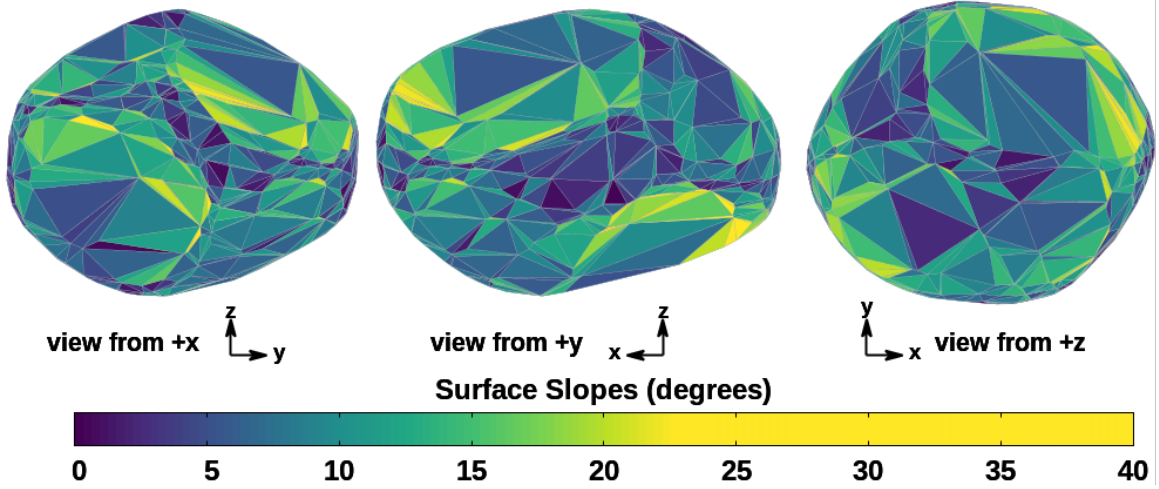


**Figure 16.** Surface slopes mapped on the surface of Justitia considering the Mars gravitational perturbation at 1.08 au distance from asteroid Justitia, respectively.

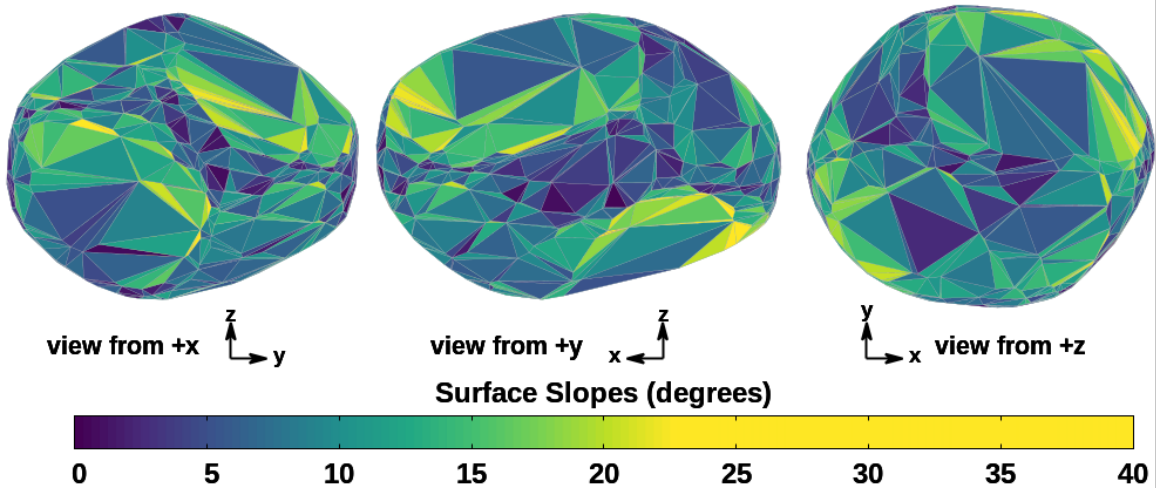


**Figure 17.** Surface slopes mapped on the surface of Justitia considering the Jupiter gravitational perturbation at 2.61 au distance from asteroid Justitia, respectively.

of its shape, in which an equivalent ellipsoid approximates its gravitational potential.

We use the inertia momentum constrained by the 3-D polyhedral surface and computed numerically to infer the ellipsoidal dimensions ( $a$ ,  $b$ , and  $c$  semi-axes) of the asteroid Justitia, given an “equivalent ellipsoidal” shape (Dobrovolskis 1996). Also, the parameters  $\mathcal{K}$ ,  $M$ , and  $R$ , discussed in the following paragraphs, were obtained from the original 3-D polyhedral shape model. To this end, the potential was expanded as a series of spherical harmonics up to fourth order, providing an approximate representation of the gravitational perturbations associated with its irregular shape. The adoption of the simplified model reduces the computational cost involved in the analysis.

Writing the effective potential  $V$  in Cartesian coordinates, as given by Eq. (14), where  $r = \sqrt{x^2 + y^2 + z^2}$  represents the distance from the point to the center of the asteroid, and  $C_{nm}$ , with  $n$  and  $m$  being the degree and order of the expansion, respectively, represent the spherical harmonic coefficients derived from the polyhedral model described in Section 3 and listed in Table 5. The dimensionless parameter  $\mathcal{K}$  corresponds to the ratio between gravitational acceleration and centrifugal acceleration.

$$\mathcal{K} = \frac{GM}{\omega^2 R^3} \in (0, \infty), \quad (13)$$

where  $\mathcal{K} < 1$  means fast rotation of the asteroid, and  $\mathcal{K} > 1$  means slow rotation (Riaguas et al. 2001).  $G$  the gravitational constant,  $M$  the total mass of the asteroid,  $R$  the equatorial radius, and

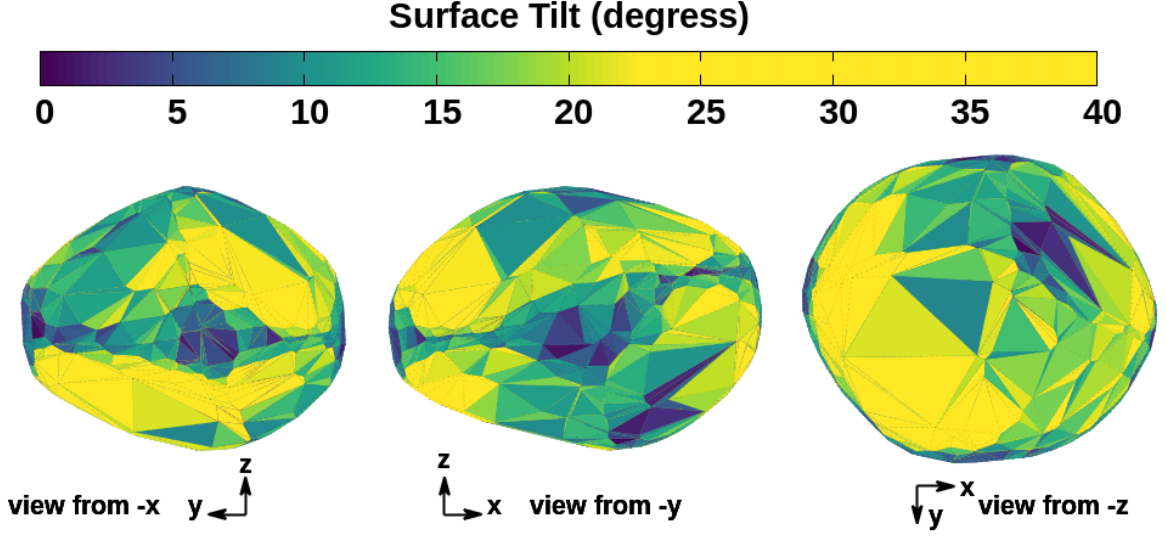


**Figure 18.** Surface tilt is mapped across the surface of Justitia, considering its 3-D polyhedral shape model with 574 vertices and 1,144 faces. The color code gives the surface tilt in degrees.

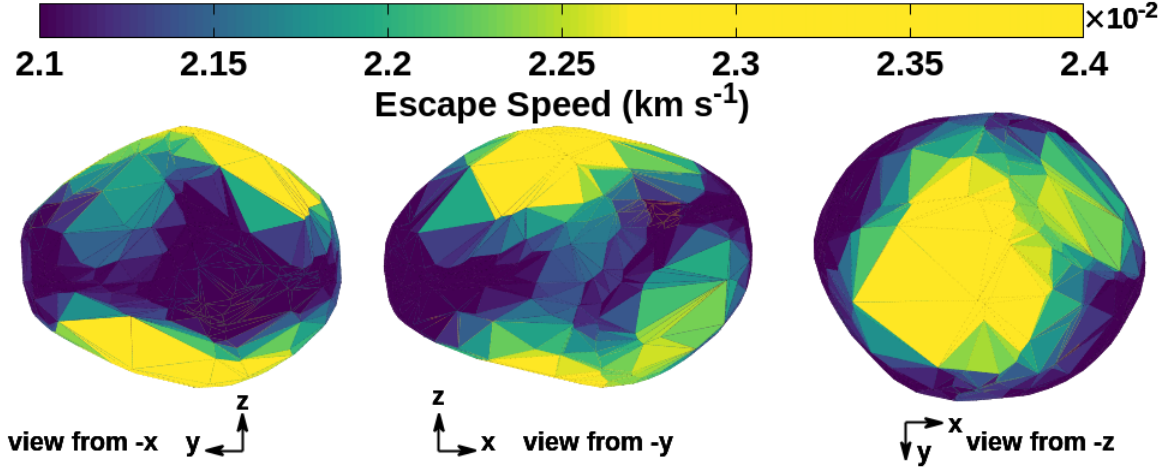


**Figure 19.** Local normal escape speed  $v_e$  calculated over the surface of Justitia, in  $\text{km s}^{-1}$ , from three perspectives:  $-x$ ,  $-y$ , and  $-z$ . The color box denotes the values of escape speed.

$\omega$  the angular speed are all presented in Tab. 6.

$$\begin{aligned}
 V = & \frac{1}{2}(x^2 + y^2) \\
 & + \frac{\mathcal{K}}{r} \left[ 1 - \left(\frac{1}{r}\right)^2 \left( \frac{C_{20}(x^2 + y^2 - 2z^2)}{2r^2} + \frac{3C_{21}xz}{r^2} - \frac{3C_{22}(x^2 - y^2)}{r^2} \right) \right. \\
 & + \left(\frac{1}{r}\right)^3 \left( \frac{C_{30}z(-3x^2 - 3y^2 + 2z^2)}{2r^3} + \frac{3C_{31}x(x^2 + y^2 - 4z^2)}{2r^3} \right. \\
 & \left. \left. + \frac{15C_{32}(x^2 - y^2)}{r^3} - \frac{15C_{33}x(x^2 - 3y^2)}{r^3} \right) \right. \\
 & + \left(\frac{1}{r}\right)^4 \left( \frac{C_{40}(3(x^2 + y^2)^2 - 24(x^2 + y^2)z^2 + 8z^4)}{8r^4} \right. \\
 & + \frac{5C_{41}xz(3x^2 + 3y^2 - 4z^2)}{2r^4} - \frac{15C_{42}(x^2 - y^2)(x^2 + y^2 - 6z^2)}{2r^4} \\
 & \left. \left. - \frac{105C_{43}xz(x^2 - 3y^2)}{r^4} + \frac{105C_{44}(x^4 - 6x^2y^2 + y^4)}{r^4} \right) \right].
 \end{aligned}$$

Considering the rotational frame system, where the asteroid is centered on its center of mass and aligned

with its main axis of inertia, being the equation that describes the movement dimensionless of a point around the asteroid, after the transformations  $t \rightarrow \omega\tau$  and  $\mathbf{r} \rightarrow R\mathbf{r}$ , given by Eq. (15). Note that the time and length scales chosen in the transformation are equivalent to  $1/\omega$  as the unit of time and  $R$  as the unit of length.

$$\begin{aligned}
 \ddot{x} - 2\dot{y} &= \frac{\partial V}{\partial x}, \\
 \ddot{y} + 2\dot{x} &= \frac{\partial V}{\partial y}, \\
 \ddot{z} &= \frac{\partial V}{\partial z}.
 \end{aligned} \tag{14}$$

In this study, we aim to explore planar symmetric periodic orbits (SPO) around asteroid Justitia using the

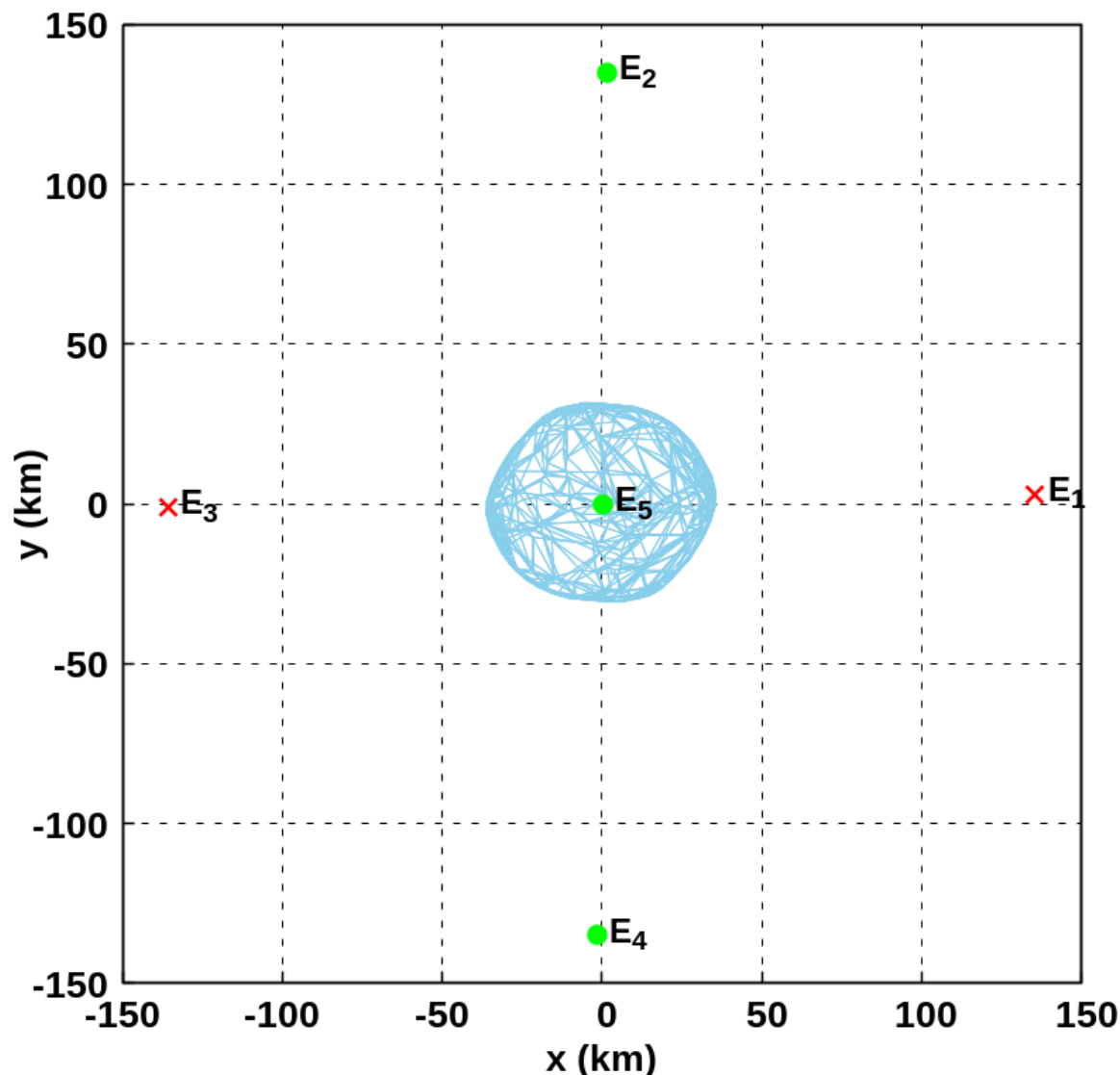


**Figure 20.** Location and stability of the five equilibrium points about asteroid Justitia are projected onto the  $xOy$  plane. The crosses points denote saddle-center-center points, which are hyperbolically unstable due to their saddle-like topology. In contrast, the circles points represent center-center-center points, indicating linear stability.

Grid Search Method (Markellos et al. 1974; Russell 2006; Tsirogianis et al. 2009; Barrio & Blesa 2009). From a mathematical standpoint, a system exhibits periodic solutions if, for the differential equation as in Eq. (15), there exists a particular solution satisfying  $(x(t_0), \dot{x}(t_0)) = (x(t_0 + T), \dot{x}(t_0 + T))$ , where  $T > 0$  represents the period. This means that the initial state  $(x(t_0), \dot{x}(t_0))$  repeats after time  $T$ , such that  $(x(t) = x(t + T), \dot{x}(t) = \dot{x}(t + T))$ . Specifically, when  $\dot{x}(t_0) = \dot{x}(t_0 + T) = 0$ , the solution represents a symmetric periodic orbit, with the velocity being perpendicular to the axis of motion. For the equation (15), the system is symmetric under the transformation  $(x, y, \dot{x}, \dot{y}; t) \rightarrow (x, -y, -\dot{x}, \dot{y}; -t)$ . Thus, an orbit with initial conditions  $(x_0, y_0, \dot{x}_0, \dot{y}_0) = (x_0, 0, 0, \dot{y}_0)$  will cross the  $x$ -axis at

$t = 0$  and again at  $t = T/2$ , under identical conditions, meaning  $y(x_0, 0, 0, \dot{y}_0; T/2) = x(x_0, 0, 0, \dot{y}_0; T/2) = 0$ . Consequently, the orbit is closed and symmetric with respect to the  $x$ -axis.

*Grid Search Method* – After identifying a symmetric periodic orbit, various methods can be applied to determine the corresponding family (Deprit & Henrard 1967; Lara et al. 1995). The Grid Search Method provides a straightforward and systematic approach for computing the whole families of periodic orbits in non-integrable systems within a specific region of the relevant initial condition space. This method can be enhanced by additional data-processing techniques for classifying periodic

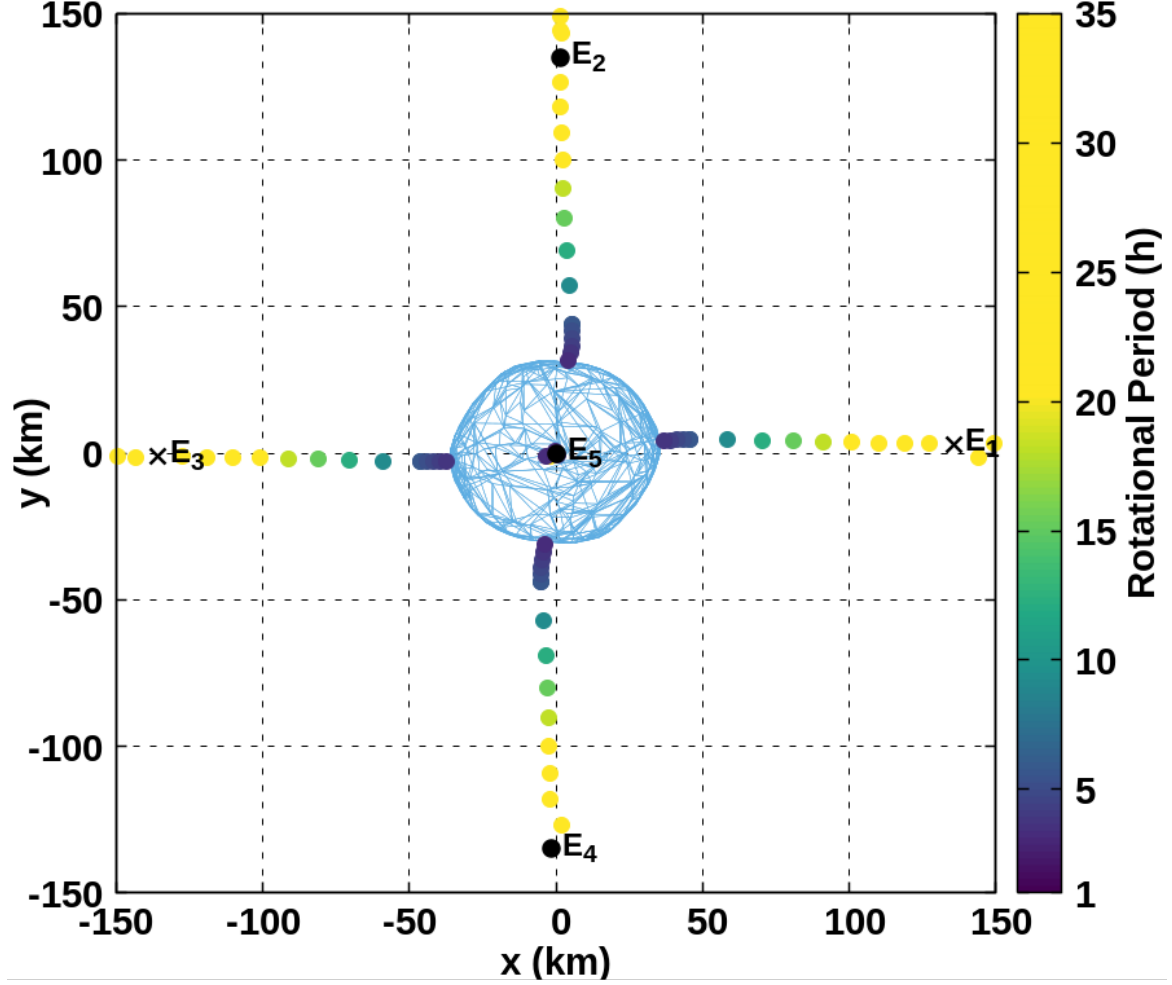


**Figure 21.** Distribution of equilibrium points around a slowly rotating body, showing how they approach the body as the rotational period increases. The positions of the five original equilibrium points around Justitia are in black. Each colored point represents the equilibrium position for a given rotational period, as indicated by the colored bar on the right (in hours). In the center of the image, a representation of the surface of Justitia.

orbits (Markellos et al. 1974; Russell 2006; Tsirogiannis et al. 2009; Barrio & Blesa 2009).

Starting with the Jacobi constant  $J = 2V(x, y) - (\dot{x}^2 + \dot{y}^2)$ , a grid was created based on the integral of motion ( $J$ ) and spatial variables. In this context, the pair  $(x, J)$  defines a complete set of initial conditions, where  $y_0 = \dot{x}_0 = 0$  and  $\dot{y}(x, J)$ . For each set of initial conditions  $(x, J)$ , the equation of motion (15) is numerically integrated to compute the Poincaré map (crossing the  $x$ -axis with  $\dot{y} > 0$ ). Upon obtaining the Poincaré map, the sign of  $\dot{x}$  is checked, and using continuity, if  $\dot{x}(t_0 + n\Delta t) < 0$  and  $\dot{x}(t_0 + (n + 1)\Delta t) > 0$ , a root-finding procedure is applied in conjunction with the numerical integrator (Brent 1971). Once convergence is reached, the initial conditions for the symmetric periodic orbit are considered satisfied. The final check involves integrating the initial conditions up to the full period  $T$ , and verifying whether  $\|(x, 0, 0, \dot{y}) - (x(pT), \dot{x}(pT), y(pT), \dot{y}(pT))\| <$

$P_{\text{tol}}$ , where  $p$  is a multiple of the complete period  $T$  and  $P_{\text{tol}}$  is the tolerance. Initial conditions that do not meet this final check are discarded.

*Topological Classification* - The topological classification facilitates the identification of the main characteristics of the families without requiring direct visualization of the orbits (Abad et al. 2023). It reveals the features standard to all orbits within a family, as well as the variations that occur at the endpoints of each curve, based on the specific points encircled by the orbit—namely, the asteroid (denoted by  $B$ ) and the equilibrium points, whose locations correspond to those depicted in Fig. 22(a), with  $E_2$  and  $E_4$  representing the triangular points, collectively denoted by the single letter  $E_{2,4}$ .

Additionally, this classification system considers the orbital motion’s sense: “Direct ( $\mathcal{D}(\quad)$ )”, refers to cases

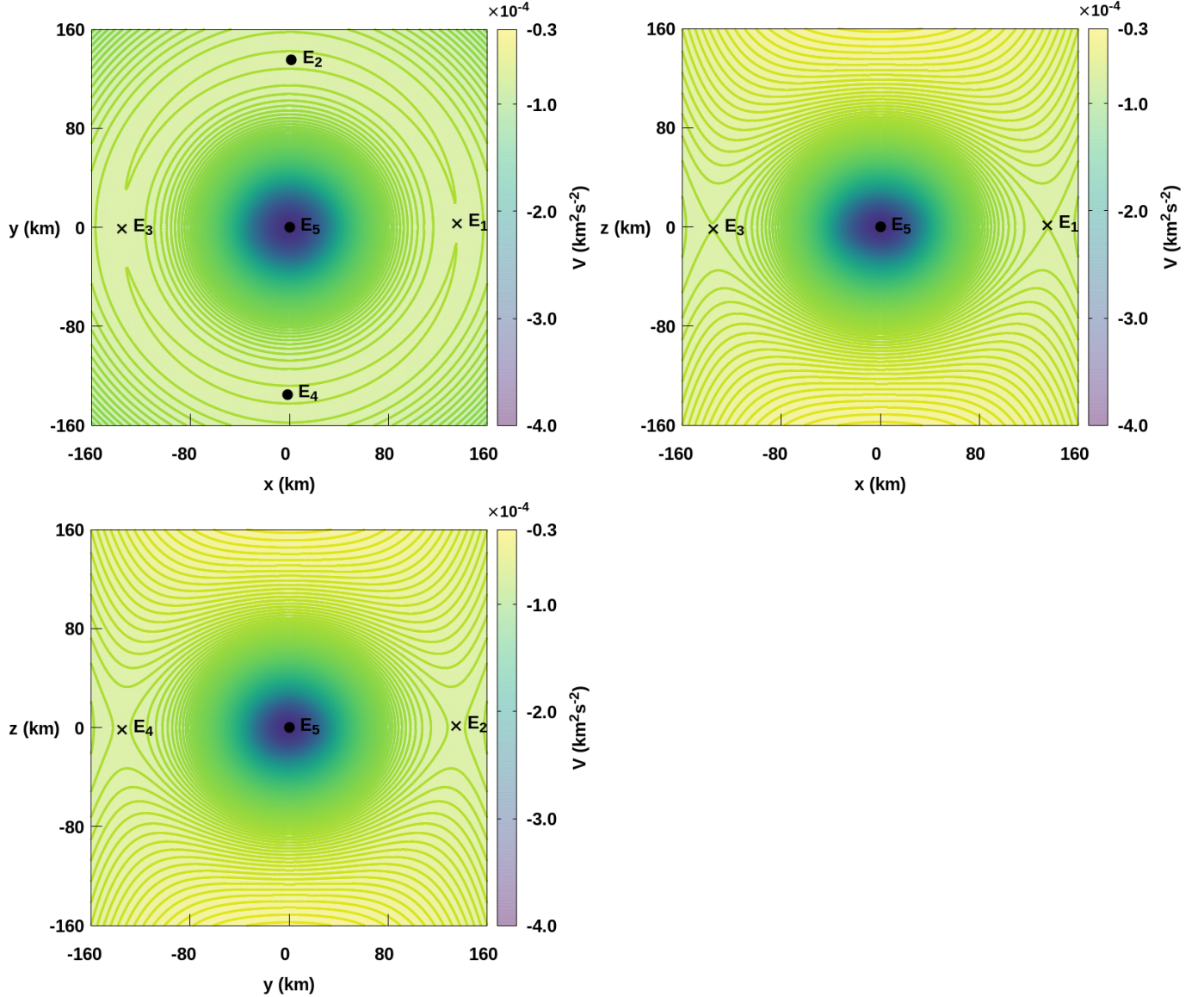


**Figure 22.** Plot of Justitia’s  $V(\mathbf{r})$  in the  $xOy$ ,  $xOz$ , and  $yOz$  planes, respectively. The color bar illustrates the zero-velocity curves of Justitia’s Jacobi constant  $J$ , in  $\text{km}^2\text{s}^{-2}$ . The dots represent the equilibrium point locations for a rotational period of **33.12962** h and a density of  $1\text{ g cm}^{-3}$ .

where  $x_0 > x_{T/2}$ , with  $x_{T/2}$  defined as the  $x$ -coordinate at half the period  $T$  where the trajectory crosses the  $x$ -axis perpendicularly, and “Retrograde ( $\mathcal{R}(\quad)$ )”, applies to cases where  $x_0 < x_{T/2}$ . Consequently, the notation  $[\quad]$  indicates that all orbits within the family exhibit similar features;  $[\rightarrow \dots]$  denotes that the orbits at one end retain the general family characterization while differing at the opposite end; and  $[\dots \rightarrow \dots]$  signifies that both ends diverge from the typical characterization. It is worth noting that, in Tab. 7, the common term of each representation is emphasized in boldface.

*Stability of the orbit* - The linear stability of an orbit refers to the analysis of the system’s response to small

perturbations around a periodic solution, made through the linearization of the equations of motion (Eq. (15)), that is, it indicates whether minor variations in the position or velocity of the asteroid are amplified, remain constant, or decay over time.

The stability of a periodic orbit is determined by analyzing the eigenvalues of the monodromy matrix associated with the orbit, which correspond to the modes that govern the linear behavior near the periodic trajectory.

The monodromy matrix of an orbit,  $M = \Phi(t_0+T, t_0)$ , is obtained by integrating the state transition matrix  $\dot{\Phi} = A(t)\Phi(t, t_0)$  for a complete period  $T$  (Parker & Anderson 2014), since  $A(t)$  is the Jacobian matrix (Eq. (16)),  $V_{xx}, V_{xy}, V_{yx}, V_{yy}$  the second derivative of

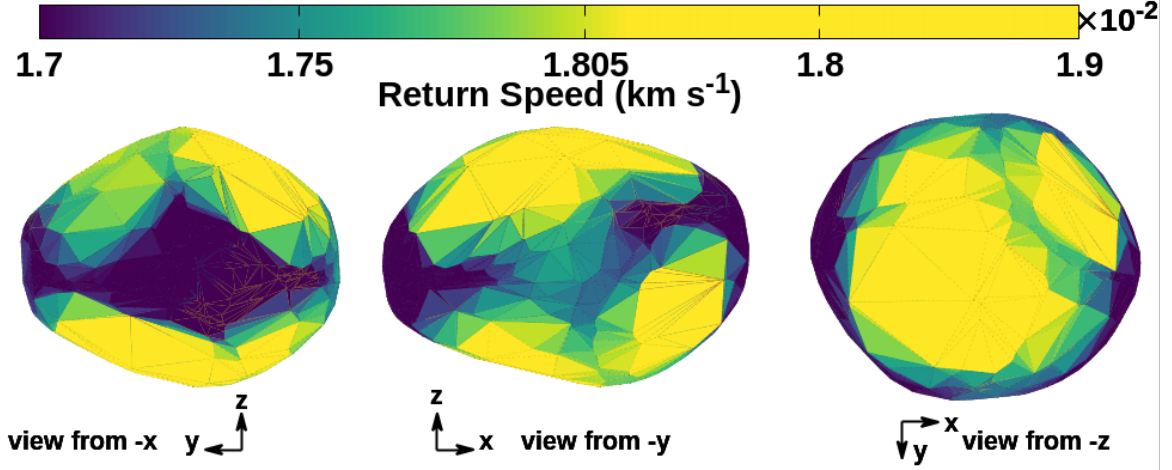


**Figure 23.** Return speed computed across the surface of asteroid Justitia. The color box denotes the values of Return speed, in  $\text{km s}^{-1}$ .

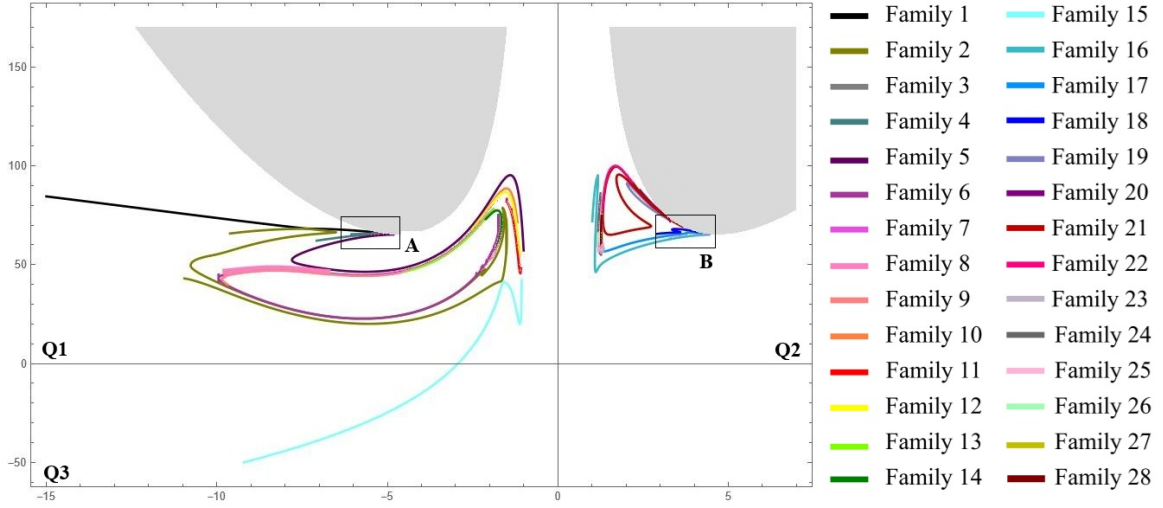


**Figure 24.** Characteristic curves of the asteroid (269) Justitia, considering the density equal to  $1.0 \text{ g cm}^{-3}$ . Each curve, represented by a distinct color and named according to the legend, corresponds to a family of symmetric periodic orbits (SPO). Each point along a given SPO family represents the initial condition of an orbit. The  $x$ -axis is the initial position at  $x_0$  of the orbit at time  $t = 0$ ; the  $y$ -axis, the Jacobi constant ( $J$ ). The map is divided into quadrants Q1, Q2 and Q3, with regions A (Fig. 25a) and B (Fig. 25b) indicating close view areas.

the effective potential (Eq. (14)) and the state transition matrix in the initial time equal to the identity matrix,  $\Phi(t_0, t_0) = I_{4 \times 4}$ . It provides information about all regions the particle traverses along its orbital path.

$$A(t) = \begin{bmatrix} 0 & 0 & 1 & 0 \\ 0 & 0 & 0 & 1 \\ V_{xx} & V_{xy} & 0 & 2 \\ V_{xy} & V_{yy} & -2 & 0 \end{bmatrix}. \quad (16)$$

In the planar case, the monodromy matrix has four eigenvalues and their corresponding eigenvectors. Due to the symplectic structure of the system, the eigenvalues appear in reciprocal pairs, and, as a consequence of

the periodicity of the solution, two of them are equal to one, so  $\lambda_1, \lambda_2 = \frac{1}{\lambda_1}, \lambda_3 = 1, \lambda_4 = 1$ . Therefore, the characteristic polynomial is

$$P(\lambda) = \lambda^4 - (k - 2)\lambda^3 + (2 + 2k)\lambda^2 - (2 + k)\lambda + 1, \quad (17)$$

since  $k = |\lambda_1 + \frac{1}{\lambda_1}|$  the stability index. This index is a single metric to assess the stability of the system (Parker & Anderson 2014):

- $k > 2$  the orbit is unstable;
- $k = 2$  the orbit is neutrally stable;
- $k < 2$ , the orbit is linearly stable.

**Table 5.** Normalized spherical harmonics coefficients of (269) Justitia’s gravity field up to degree and order four, derived from the polyhedral shape model (Werner 1997). The coefficients are computed using a reference radius of  $R = 29.0$  km and density of  $1.0 \text{ g cm}^{-3}$ . The reference frame is centered at the center of mass and aligned with the principal axes of inertia.

Order (n)	Degree (m)	$C_{n,m}$
0	0	1.0
1	0	0
1	1	0
2	0	$-5.44305 \times 10^{-2}$
2	1	0
2	2	$2.410451 \times 10^{-2}$
3	0	$2.33221 \times 10^{-3}$
3	1	$4.32010 \times 10^{-2}$
3	2	$3.04401 \times 10^{-3}$
3	3	$-1.26468 \times 10^{-3}$
4	0	$1.39609 \times 10^{-2}$
4	1	$-5.76107 \times 10^{-3}$
4	2	$-5.38729 \times 10^{-3}$
4	3	$1.85068 \times 10^{-3}$
4	4	$8.98077 \times 10^{-3}$

**Table 6.** Parameters of (269) Justitia, being  $M$  the total mass of the asteroid,  $R$  the equatorial radius, and  $\mathcal{K}$  the dimensionless parameter.

$M$ (kg)	$R$ (km)	$\omega$ (rad/s)	$\mathcal{K}$
$1.021604 \times 10^{17}$	29.0	$5.26818 \times 10^{-5}$	100.73314

### 13.1. Symmetric Periodic Solutions

In autonomous Hamiltonian systems, periodic orbits appear in families, represented by characteristic curves (smooth one-parameter continuous curves), as in Fig. 24. Each point in the families, represented on the axes  $(x_0, J)$ , is the initial condition of an SPO. Note that 28 families were found, represented by different colors, and distributed between quadrants  $Q1$ ,  $Q2$ , and  $Q3$ . The asteroid is arranged on the  $x$ -axis, from  $-1$  to  $1$ , since the unit of distance is its equatorial radius. The gray region, limited by  $J = 2V$  for  $y = 0$ , is physically forbidden due to the negative speed of the particle orbiting the asteroid. The rectangles  $A$  and  $B$ , highlighted on the map, are shown at higher magnification in Figs. 25a and 25b, respectively.

Note, in Tab. 7, that Families 1, 3, and 4 have the same topological characterization; all of them surround the collinear and triangular equilibrium points and the asteroid. The difference between them lies in the loops

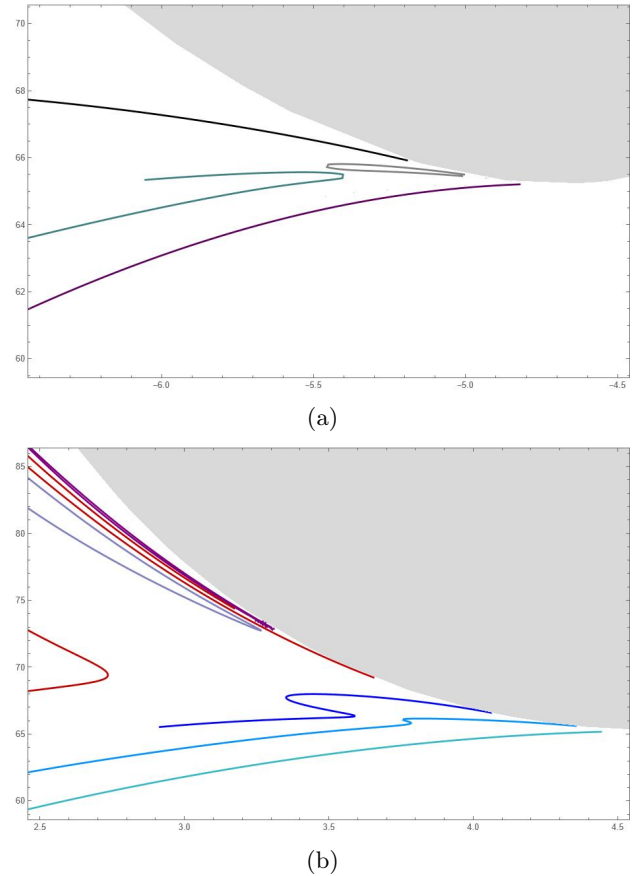


**Figure 25.** Closer view of the regions highlighted by (a) rectangle A, and (b) rectangle B, in Fig. 24.

that appear when families change. A loop occurs when the periodic orbit presents one or more self-intersections in the configuration space, that is, there exists at least one pair of instants  $t_1 \neq t_2 \in [0, T]$  such that,

$$x(t_1) = x(t_2),$$

since the same point is crossed more than once, but in different directions, characterizing the loop. To exemplify this behavior, see the evolution of the orbits of Families 1, 3, and 4 in Figs. 26a, 26b, 26c. This work focuses on the search and presentation of orbit families; therefore, a study of the reasons for their occurrence and characterization will not be presented.

Regarding the linear stability of the orbits, Figs. 27a, 27b, 27c, for the cases in Figs. 26a, 26b, 26c, presents the stability index  $k$  as a function of the initial condition  $x_0$ , with the red dashed line on the graph at the limit  $k = 2$ . When the stability index  $k = 2$ , the periodic orbit is in a critical condition, which marks the limit between linear stability ( $k < 2$ ) and instability ( $k > 2$ ). In this situation, it does not characterize instability but rather a transition point where small variations in the

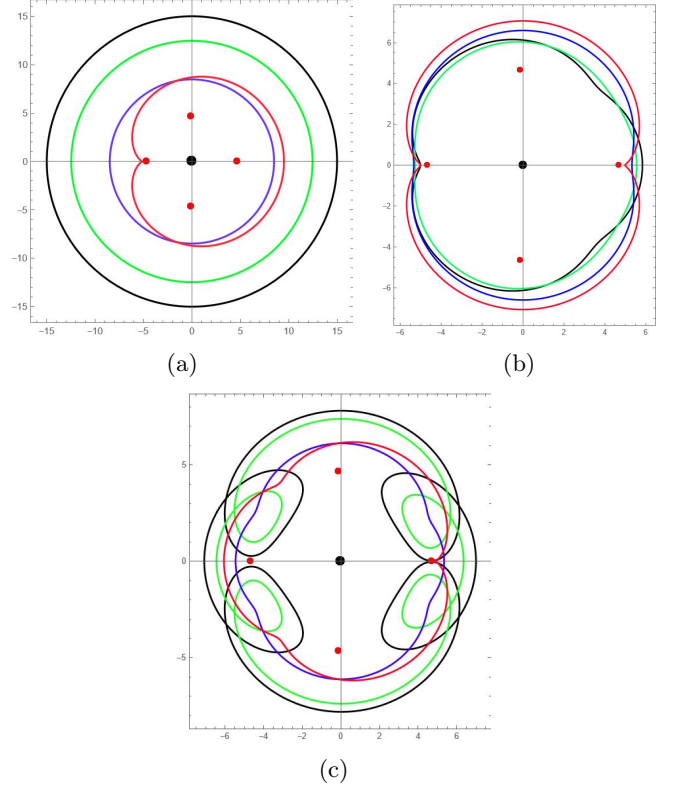
**Table 7.** Topological characterization of families of SPO for the asteroid Justitia

Region	Curves	Topological characterization
Q1	Families 1, 3, 4	$\mathcal{R}(E_3 \ B \ E_1 \ E_{2,4}) [ \ ]$
	Family 2	$\mathcal{R}(B) [\{E_1, E_3, E_{2,4}\} \rightarrow \{E_1, E_3\} \rightarrow \{E_1, E_{2,4}\} \rightarrow \{E_1\} \rightarrow \rightarrow \{E_3\} \rightarrow \{E_3, E_{2,4}\}]$
	Family 5	$\mathcal{R}( \ ) [E_3 \rightarrow \ ]$
	Family 6	$\mathcal{R}(B) [ \rightarrow \{E_3\} \rightarrow \{E_1, E_{2,4}\}]$
	Families 7, 8	$\mathcal{R}(E_3 \ B \ E_{2,4}) [ \ ]$
	Family 9	-
	Family 10	$\mathcal{D}( \ ) [ \ ]$
	Family 11	$\mathcal{R}(B) [ \rightarrow \{E_{2,4}\}]$
	Family 12, 14	$\mathcal{R}( \ ) [ \ ]$
	Family 13	$\mathcal{R}(B) [ \ ]$
Q1 and Q3	* Family 15	$\mathcal{R}(B)[\{E_1, E_3, E_{2,4}\} \rightarrow \rightarrow \{E_1\} \rightarrow \{E_1, E_{2,4}\}]$
Q2	Family 16	$\mathcal{R}( \ ) [ \rightarrow \{E_3\}]$
	Families 17-19, 21-23, 26	$\mathcal{D}(B) [ \ ]$
	Families 20,24-25,27-28	$\mathcal{D}( \ ) [ \ ]$

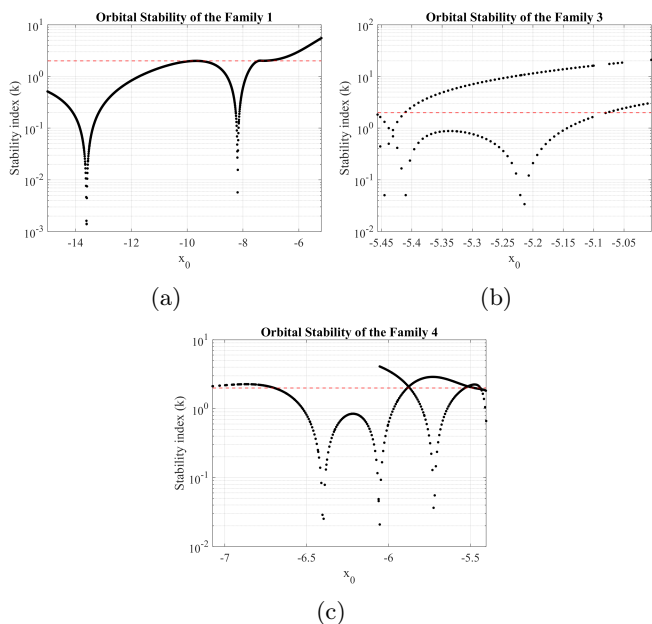
system parameters can qualitatively change the behavior of the solutions. Note that the families in Figs. 27a, 27b, 27c have a significant part of stable orbits, with some unstable parts, with  $k$  around 10.

Figure 28 shows the evolution of Family 2, which has an initial condition at point 1 (green) in Fig. 28a, and the orbit evolves according to Fig. 28b. Points 2 to 7 in Fig. 28a (red points) are the initial conditions of the orbits in Fig. 28c to Fig. 28g. Notice that Orbit 2 closes a loop at the triangular equilibrium points, and subsequently, in Orbit 3, the loop no longer encircles these points. Continuing the evolution, in Orbit 4, the left side of the orbit ( $x < 0$ ) decreases significantly in relation to the right side ( $x > 0$ ) until the orbit encircles points  $E_1$  and the triangular points, as well as the body, leaving out equilibrium point  $E_3$ . Continuing, in Orbit 5, the loop disappears, the amplitude of the right side of the orbit decreases until it no longer involves the triangular equilibrium points, remaining only around  $E_1$ . Then the amplitude of the left side increases, while the amplitude of the right side of the orbit decreases, encircling only the body and point  $E_3$ . Finally, the family is completed by Orbit 7 (in blue), represented in Fig. 28h. Note that this family has seven variations of topological orbital features, in addition to the common feature (see Tab. 7). The topological classification of this case, as well as Families 6 and 15, which also vary similarly, differs slightly from *Abad et al. (2023)* characterization method, which is limited to two variations in addition to the common part of the orbit; therefore, an adaptation of this method was made for these cases.

Regarding the stability of Family 2, see Figure 29, which shows that there are stable and unstable cases,



**Figure 26.** Evolution of the orbits of families (a) 1, (b) 3, and (c) 4. Black and red orbits are the ends of the families, and green and blue are intermediate points. The black dot represents the asteroid Justitia (not to scale), and the red dots are the equilibrium points. The abscissa and ordinate axes are the components of the particle's position around the asteroid, in  $x$  and out  $y$ , respectively.



**Figure 27.** Stability index referring to families: (a) 1, (b) 3, and (c) 4. The dashed red line at  $k = 2$ .

with the majority being unstable. The orbits resulting from initial conditions 1 to 7, shown in Fig.28a, are all unstable; the initial conditions of the stable orbits are small segments between points 1 and 2 and another segment between points 5 and 6.

The behavior of the Family 5 is shown in Fig. 30. In Fig. 30a, at the top right of the figure, we have the complete Family 5 (black curve). The red point represents the limit where collision cases begin; that is, the part of the curve between the green and red points corresponds to the families considered in the topological classification. The part between the red and blue points represents all the initial conditions of the orbits that, at some point, diverged from the initial one and collided with the asteroid. At the top left, we have the evolution of the collision limit orbit.

In contrast, at the bottom, we show the evolution of the family’s initial orbit (on the left) and its final orbit (on the right), corresponding to the green and blue points of the complete curve; therefore, only the blue orbit is a collision orbit. The black and pink orbits, and all those between them (some shown in Fig. 30b), are collision-free orbits, some of which are Lyapunov type. Lyapunov orbits, in this case, emerge from the collinear Lagrange point  $E_3$ , are retrograde, and mostly unstable (as in Fig. 31). Family 16 exhibits behavior similar to Family 5, with Lyapunov-type orbits emerging from the equilibrium point  $E_1$  and without collision orbits; however, there are some cases in which it passes within 100 meters of the body’s surface. Regarding stability, there

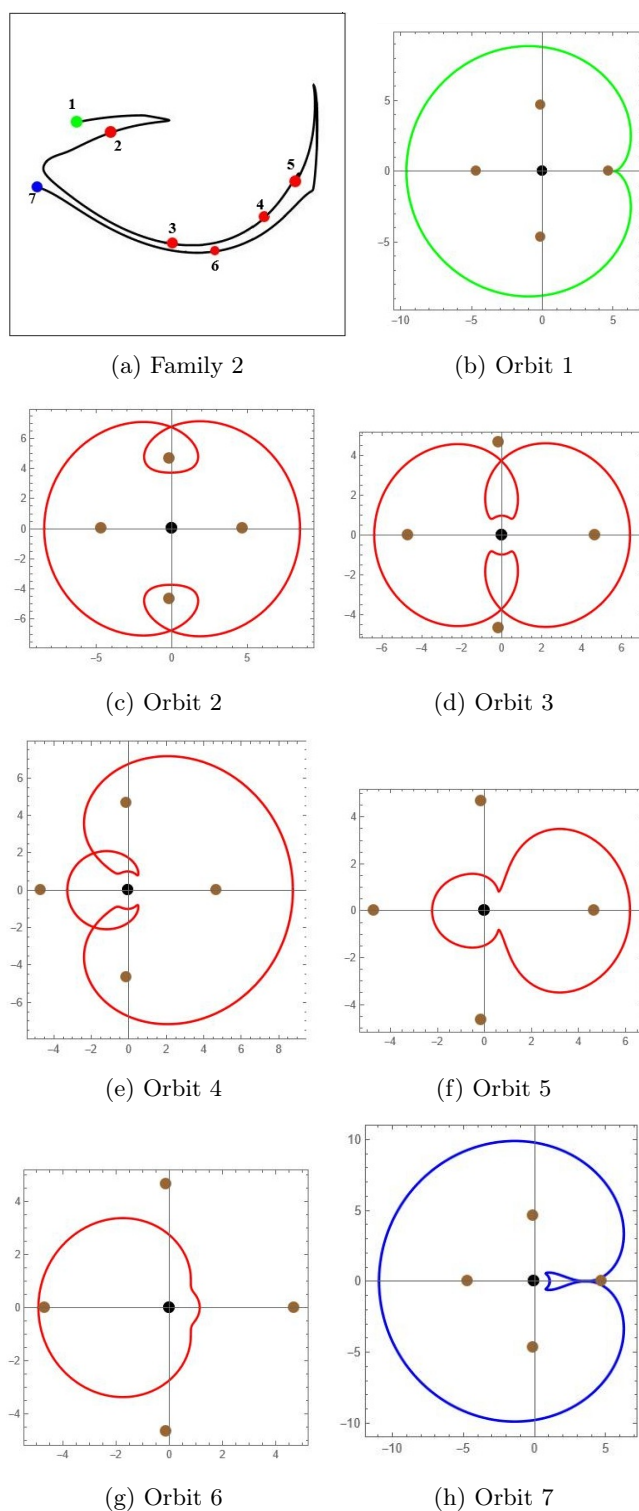


**Figure 28.** Evolution of the orbits of Family 2. Orbit 1 (green) and Orbit 2 (blue) are at the ends of the family, and red are intermediate points. The black dot represents the asteroid *Justitia* (not to scale), and the brown dots are the equilibrium points. The abscissa and ordinate axes are the components of the particle’s position around the asteroid, in  $x$  and out  $y$ , respectively.

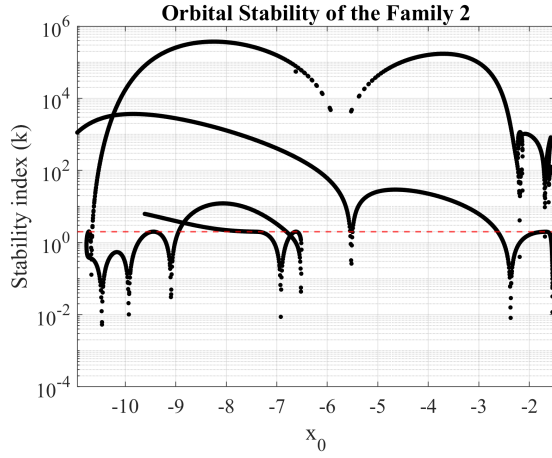


**Figure 29.** Stability index referring to Family 2. The dashed red line at  $k = 2$ .

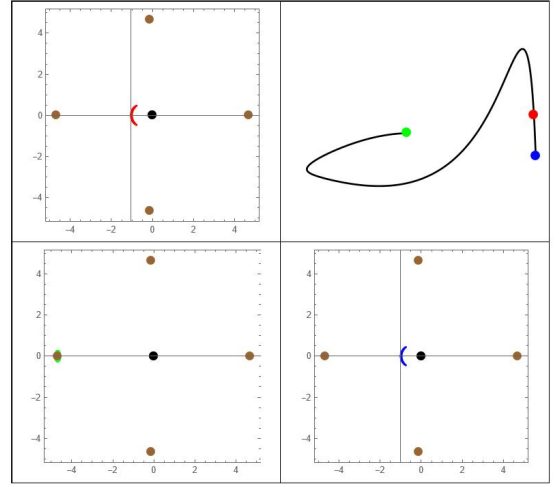
is a greater number of stable orbits compared to Fig. 31, in some cases of the Lyapunov type.

Family 6 is formed by retrograde and highly unstable orbits (see Fig. 33). According to the topological characterization (Tab. 7 and Fig. 32), the first orbit of the family is the black one, which only circles the asteroid (black dot). Representing the second characterization of the family, we have the green orbit that involves the body and the point  $E_3$ , and the blue orbit that circles the body,  $E_3$ , and the triangular points  $E_{2,4}$ . All evolution from the blue orbit resulted in a collision with the asteroid.

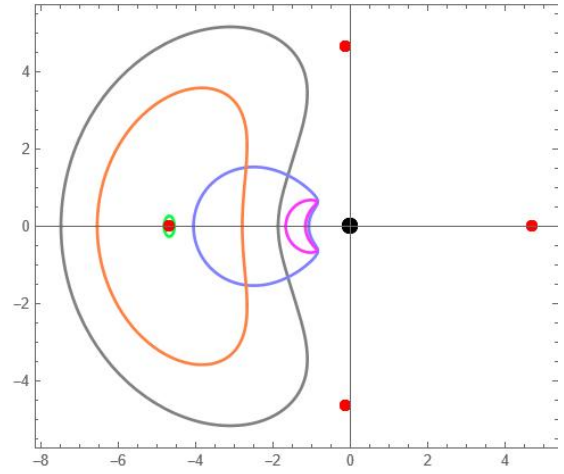
Families 7 and 8 (Fig. 34) constantly orbit the body, the equilibrium point  $E_3$ , and the triangular points. Throughout the family, this characterization remains unchanged. These are families with retrograde and highly unstable orbits. For stability, see Fig. 35.

In Table 7, there is no name for the topological characterization of Family 9, because all orbits in this family, at some point other than the initial one, collide with the asteroid. In the map of curve characteristics (Fig. 24), the Jacobi constant is around 40 or more. In these cases, the particle will have low available kinetic energy, tending to remain confined to a small region near the asteroid or, as occurred, to collide with the body. The stability indices in these cases are much greater than 2.0, which indicates highly unstable cases.

Family 11 (Fig. 36a) has a topological characterization  $\mathcal{R}(\mathbf{B}) [ \rightarrow \{E_{2,4}\}]$ , showing that as it evolves, the orbits tend to circle the triangular equilibrium points  $E_{2,4}$ , in addition to the body. Family 13 (Fig. 36b), on the other hand, orbits only the asteroid in all cases. Both families have retrograde and highly unstable orbits (see Fig. 37).



(a)



(b)

**Figure 30.** Evolution of the orbits of Family 5. (a) Top right side: The complete Family 5 curve (black curve). The red point marks the limit at which the collision cases begin. The green and blue points represent the orbits at the ends of the family. Top left: orbit of the family whose initial conditions are the green point. Bottom left: the orbit of the family whose initial conditions are the blue point. The brown points are the equilibrium points; (b) It shows five different orbits of Family 5, which are between the orbit of the initial end of the family (black) and the pink one (but free collision); the red points are the equilibrium points. The black dot represents the asteroid Justitia (not to scale). The abscissa and ordinate axes are the components of the particle's position around the asteroid, in x and out y, respectively.

Families 12 and 14 have the same topological characterization  $\mathcal{R}(\ ) [ \ ]$  (see Fig. 38), both do not encircle the body nor the equilibrium points, are retrograde and unstable (see Fig. 39).

Up to Family 14, the characteristic curves or SPO families belonged to quadrant  $Q1$ , the initial conditions

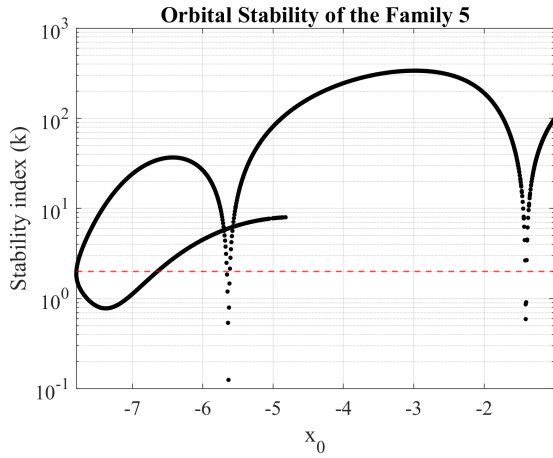


**Figure 31.** Stability index referring to Family 5. The dashed red line at  $k = 2$ .

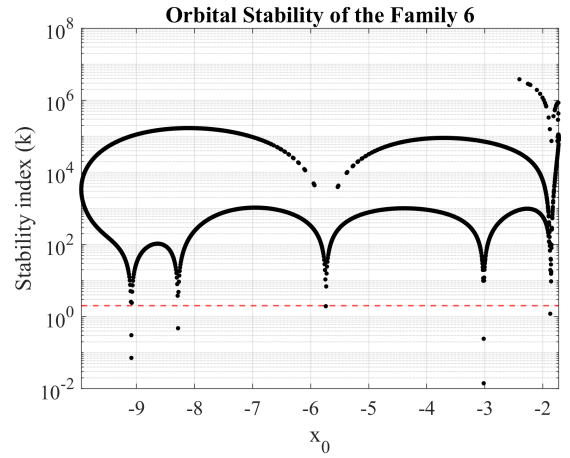


**Figure 33.** Stability index referring to Family 6. The dashed red line at  $k = 2$ .

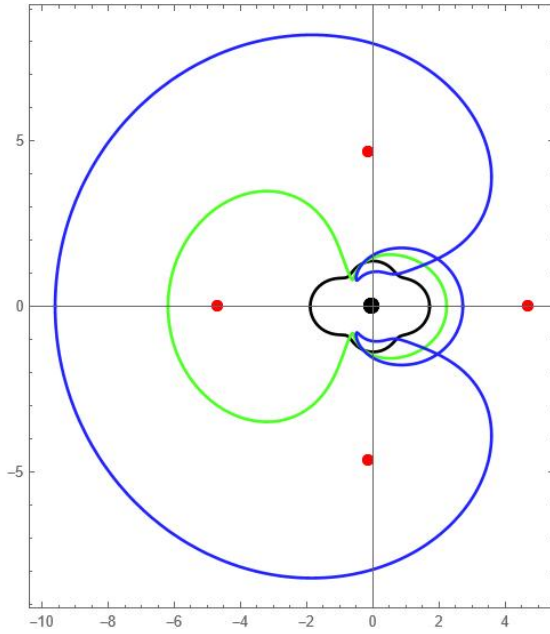


**Figure 32.** Evolution of the orbits of Family 6. Black and red orbits are the ends of the families, and green and blue are intermediate points. The black dot represents the asteroid Justitia (not to scale), and the red dots are the equilibrium points. The abscissa and ordinate axes are the components of the particle's position around the asteroid, in  $x$  and  $y$ , respectively.

map (Fig. 24). Regarding Family 15 (Fig. 40), which is divided between quadrants  $Q1$  and  $Q3$ , the topological classification (Tab. 7) has five parts in addition to the common part, in which all orbits circle the asteroid. In the first part, the black orbit in Fig. 40, involves, in addition to the body, the equilibrium points  $E_3$  and  $E_{2,4}$ ; then, the green curve orbits only the asteroid, next the body and point  $E_1$  (blue orbit); and finally, the red orbit circles the body,  $E_1$ , and the triangular points  $E_{2,4}$ .

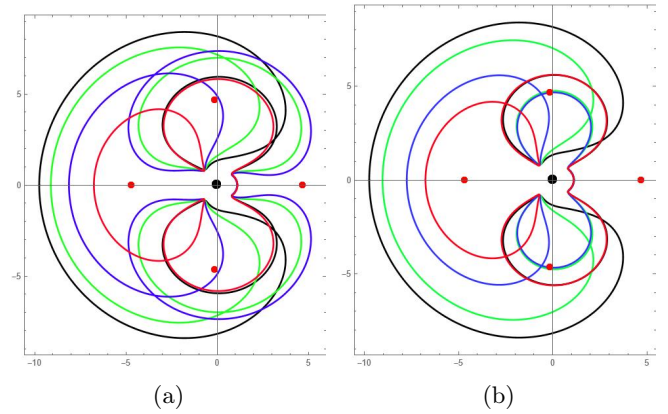


**Figure 34.** Evolution of the orbits of families (a) 7, and (b) 8. Black and red orbits are the ends of the families, and green and blue are intermediate points. The black dot represents the asteroid Justitia (not to scale), and the red dots are the equilibrium points. The abscissa and ordinate axes are the components of the particle's position around the asteroid, in  $x$  and  $y$ , respectively.

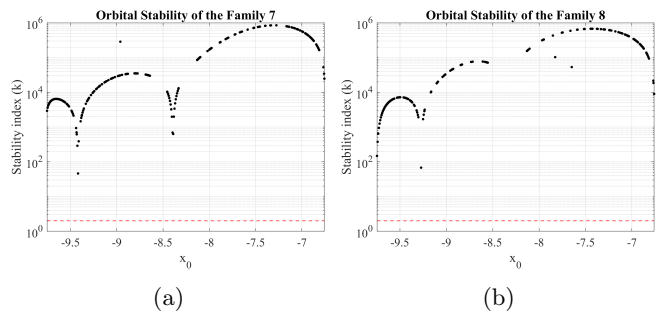


**Figure 35.** Stability index referring to Families (a) 7, and (b) 8. The dashed red line at  $k = 2$ .

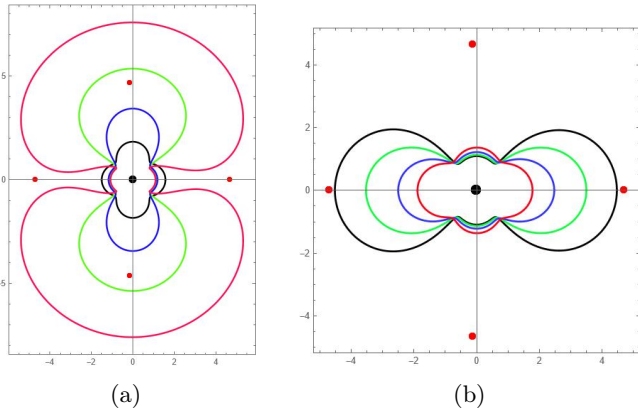


**Figure 36.** Evolution of the orbits of families (a) 11, and (b) 13. Black and red orbits are the ends of the families, and green and blue are intermediate points. The black dot represents the asteroid Justitia (not to scale), and the red dots are the equilibrium points. The abscissa and ordinate axes are the components of the particle’s position around the asteroid, in x and y, respectively.

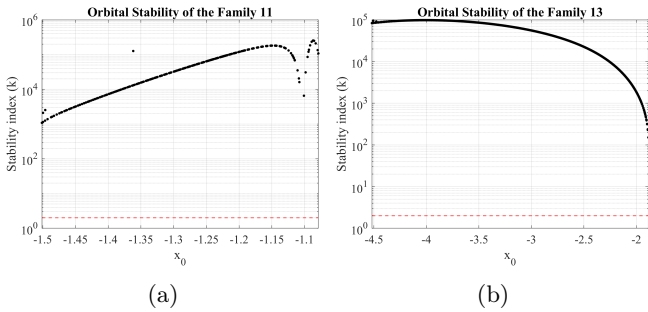


**Figure 37.** Stability index referring to Families (a) 11, and (b) 13. The dashed red line at  $k = 2$ .

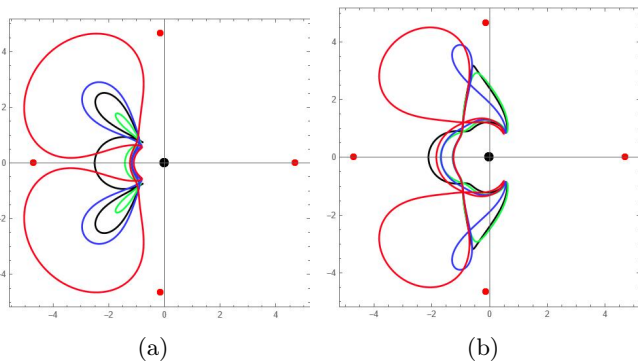


**Figure 38.** Evolution of the orbits of families (a) 12, and (b) 14. Black and red orbits are the ends of the families, and green and blue are intermediate points. The black dot represents the asteroid Justitia (not to scale), and the red dots are the equilibrium points. The abscissa and ordinate axes are the components of the particle’s position around the asteroid, in x and y, respectively.

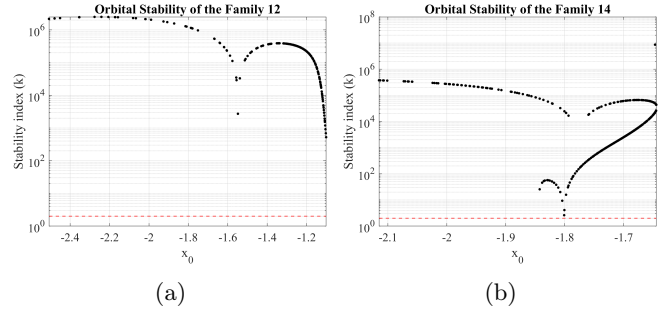


**Figure 39.** Stability index referring to Families (a) 12, and (b) 14. The dashed red line at  $k = 2$ .

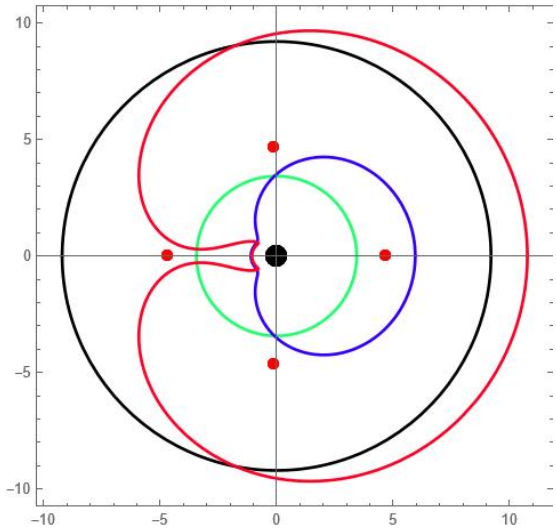


**Figure 40.** Evolution of the orbits of Family 15. Black and red orbits are the ends of the families, and green and blue are intermediate points. The black dot represents the asteroid Justitia (not to scale), and the red dots are the equilibrium points. The abscissa and ordinate axes are the components of the particle’s position around the asteroid, in x and y, respectively.

In this orbit, there are points where the distance from the body’s surface is less than 100 meters. The family is retrograde and with most of its orbits stable (see Fig. 41).

Families 17, 18, 19, 21, 22, 23, and 26 form a set of orbits that circle the asteroid Justitia only. The orbits are prograde, and some of them also tend to loop. The Fig. 42 shows the evolution of some of these families, being Fig. 42a for Family 18, 42b for Family 19, 42c for Family 22, and 42d for Family 26. Regarding the linear stability of the orbits, note in Fig. 43 that there are stable orbits in Family 18. They are not shown here, but most orbits in Families 17 and 21, which are also in this topological characterization group, are stable.

Finally, we have Families 10, 20, 24, 25, 27, and 28 with prograde, unstable orbits that do not encircle the

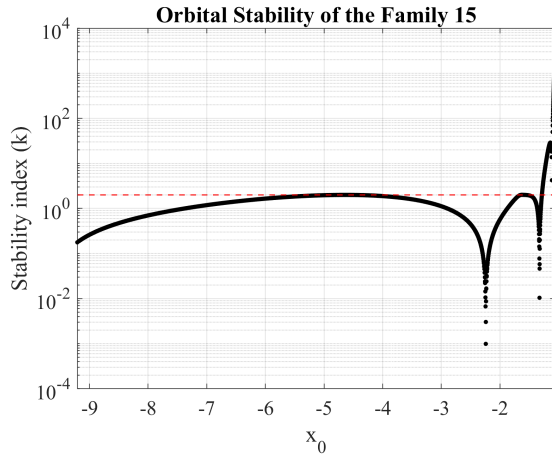


**Figure 41.** Stability index referring to Family 15. The dashed red line at  $k = 2$ .

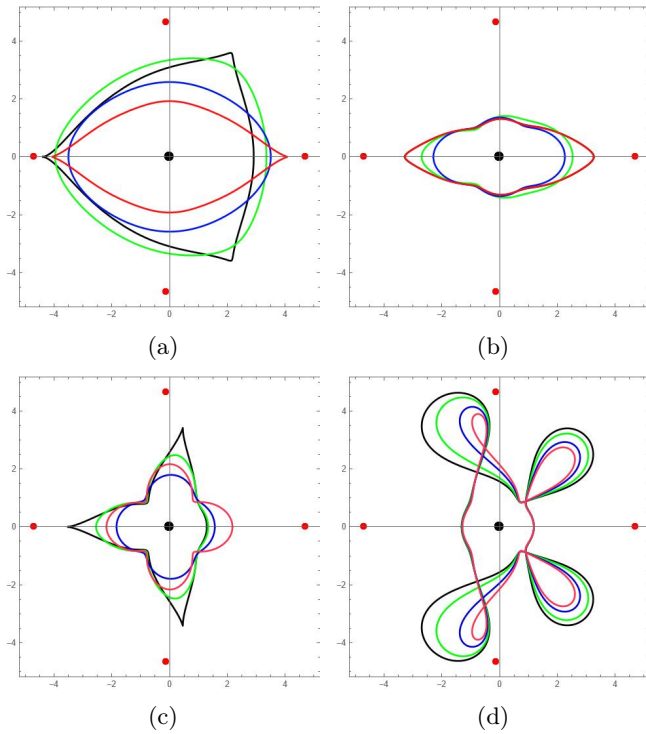


**Figure 42.** Evolution of the orbits of families (a) 18, (b) 19, (c) 22, and (d) 26. Black and red orbits are the ends of the families, and green and blue are intermediate points. The black dot represents the asteroid Justitia (not to scale), and the red dots are the equilibrium points. The abscissa and ordinate axes are the components of the particle's position around the asteroid, in  $x$  and  $y$ , respectively.

body and equilibrium points. Orbits 10 and 20 are similar, but mirror each other across the  $y$ -axis. Orbits 24, 25, 27, and 28 are also similar to each other, with some variations; they are composed of loops. To exemplify them, some will be presented in the Fig. 44. In this

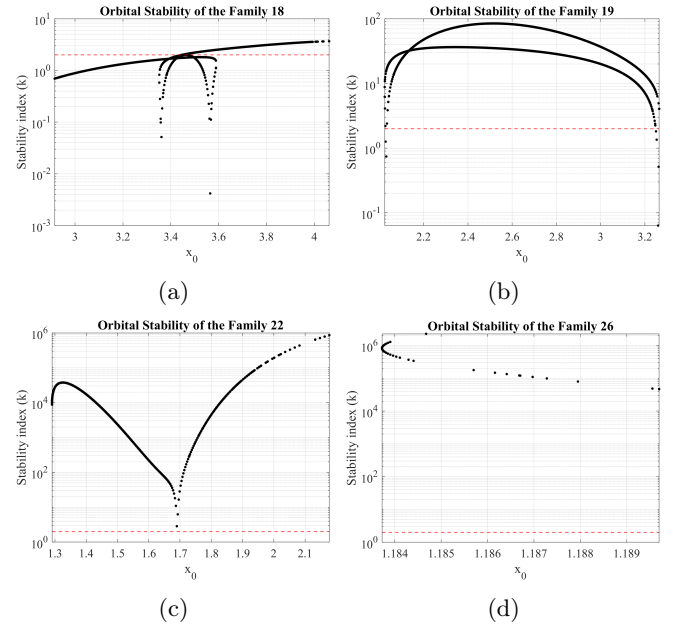


**Figure 43.** Stability index referring to families: (a) 18, (b) 19, (c) 22, and (d) 26. The dashed red line at  $k = 2$ .

group, all families are composed of highly unstable orbits, i.e.,  $k \gg 2.0$ , as shown in Fig. 45 for Families 10, 25, and 28.

The results presented so far for orbits around Justitia refer to the case with a density of  $1.0 \text{ g cm}^{-3}$ . When the density is considered to be  $2.0 \text{ g cm}^{-3}$ , changes are observed in the families of symmetric periodic orbits. Figure 46 shows the map of initial conditions of the SPO for a density of 2.0, showing a smaller number of families (24 in total) and some with different sizes compared to Fig. 24. In this figure, we highlight, using the same colors and numerical identifications, the families that exhibit behavior similar (though not identical) to that of the case with density 1.0. Of the 24 families shown in Fig. 46, only 10 maintain comparable characteristics (these are Families 1, 2, 3, 4, 5, 11, 12, 15, 16, 18), and some of them have different sizes and orbits; the remaining families, represented in green, correspond to new solutions, distinct from those obtained for density 1.0. Note also that some families have disappeared (for a density of 1.0, there were 28 families, and for a density of 2.0, there are 24).

#### 14. 3-D THERMOPHYSICAL MODEL

As we mentioned before, the EMA mission will investigate the origin and evolution of water- and carbon-rich main-belt asteroids by using three infrared sensors: a thermal infrared spectrometer (EMBIRS), a mid-wave infrared imaging spectrometer (MIST-A), and a thermal infrared imaging system (IR-cam), along with others op-

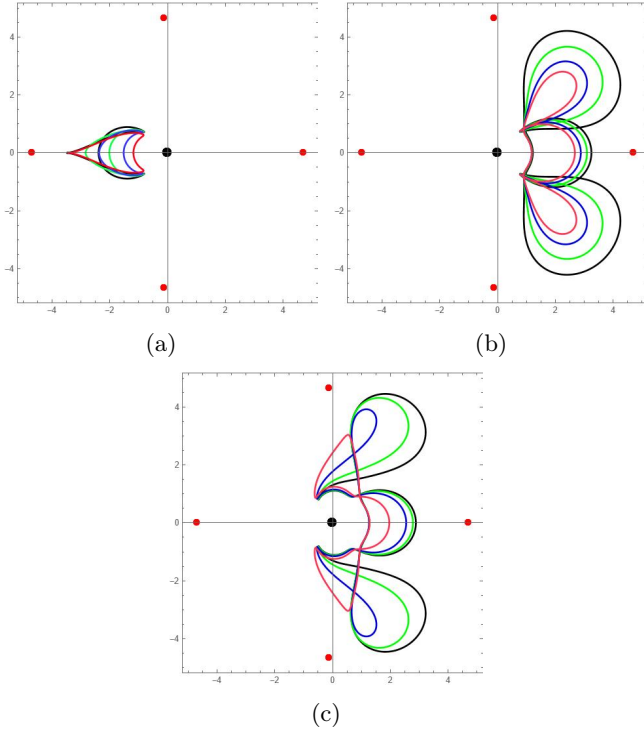


**Figure 44.** Evolution of the orbits of families (a) 10, (b) 25, and (c) 28. Black and red orbits are the ends of the families, and green and blue are intermediate points. The black dot represents the asteroid Justitia (not to scale), and the red dots are the equilibrium points. The abscissa and ordinate axes are the components of the particle’s position around the asteroid, in  $x$  and  $y$ , respectively.

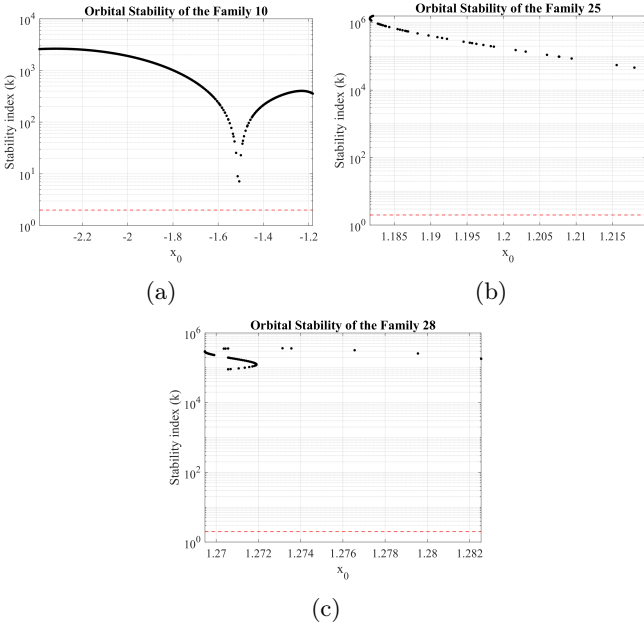


**Figure 45.** Stability index referring to families: (a) 10, (b) 25, and (c) 28. The dashed red line at  $k = 2$ .

erating in the visible wavelength range (AlSaeed et al. 2025). Justitia is a primitive asteroid with an extremely red spectral slope, consistent with either space weathering effects or an outer Solar System origin (Harish et al. 2025). In this sense, EMA will use infrared observations to determine the physical and compositional properties of the surface materials on Justitia, providing insights into its origins and geologic history.

We can estimate the surface and subsurface temperature distribution by applying the TEMPEST software (Spencer et al. 1989; Lyster et al. 2024; Lyster et al. 2025). This code calculates surface temperatures by solving the one-dimensional heat conduction equation for each facet of a shape model, using a surface energy balance that includes solar flux, thermal emission, vertical heat conduction, shadowing, radiative exchange, and (optionally) self-heating. It simulates diurnal temperature variations of a Solar System body based on a given shape model and iteratively computes insolation and temperature arrays for each facet until convergence. These results are useful for constraining the thermal properties of Justitia, such as thermal inertia, and provide insights into surface characteristics, including grain size and regolith structure.

Here, we present results of a 3-D thermophysical model incorporating the best-available shape model for asteroid Justitia, based on rotational lightcurve and stellar occultation measurements (Marciniak et al. 2025). For this analysis, we adopted an albedo of 0.06, a heliocentric distance of  $r_{\odot} = 2.6$  au (semi-major axis), a rotational period of  $P_{\text{rot}} = 33.13$  h, and ecliptic pole orientation coordinates of  $73^{\circ}$  and  $-81^{\circ}$  (Marciniak et al. 2025). We also used a bolometric emissivity of 0.9 and a bulk density of  $1 \text{ g/cm}^3$ , according to (Buie et al. 2025). We then investigated a range of thermal inertia ( $\Gamma$ ) values - 40, 100, and  $200 \text{ J m}^{-2} \text{ K}^{-1} \text{ s}^{-1/2}$  - spanning a wide range for primitive asteroids (Mueller et al. 2010; Hanuš et al. 2015). Thermal inertia is usually determined with considerable uncertainty. In Marciniak et al. (2025), it is reported as  $41_{-40}^{+110}$  SI units for Pole direction 1 (used in this simulation). According to the authors, this large uncertainty may be related to the relatively wide variations in Justitia’s heliocentric distance, since thermal inertia depends on heliocentric distance through its influence on surface temperatures. The parameter values used in the thermal analyses are summarized in Table 8.

For each thermal inertia scenario, we calculated the global distribution of surface temperatures, the diurnal amplitude at the equator, and the subsolar temperature as a function of local time. In Figure 47, we report the surface temperatures of asteroid Justitia, whose

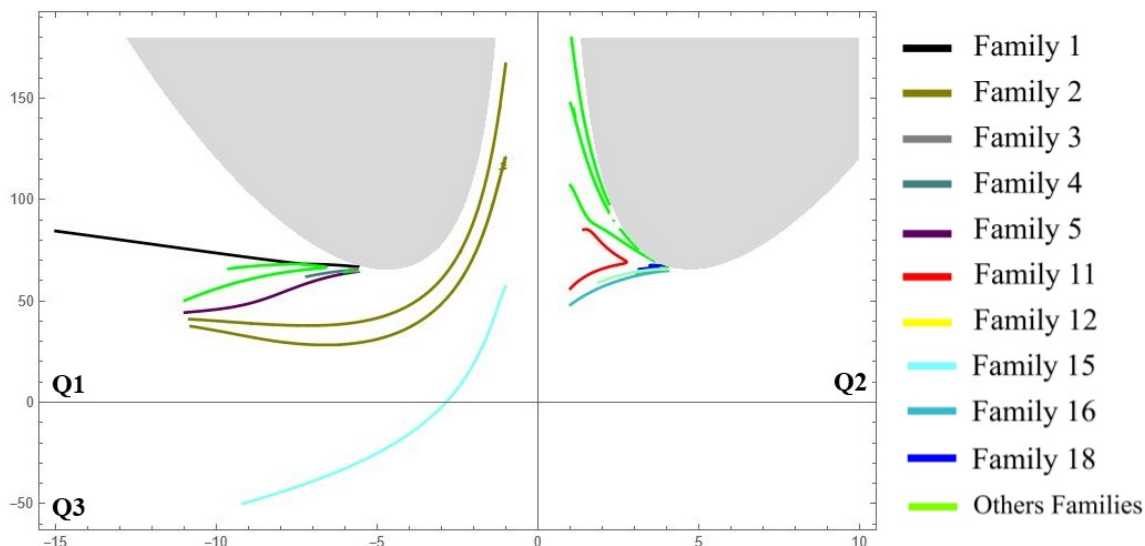


**Figure 46.** Characteristic curves of the asteroid (269) Justitia, considering the density equal to  $2.0 \text{ g cm}^{-3}$ . Each curve, represented by a distinct color and named according to the legend, corresponds to a family of symmetric periodic orbits (SPO). Each point along a given SPO family represents the initial condition of an orbit. The  $x$ -axis is the initial position at  $x_0$  of the orbit at time  $t = 0$ ; the  $y$ -axis, the Jacobi constant ( $J$ ). The map is divided into quadrants Q1, Q2, and Q3.

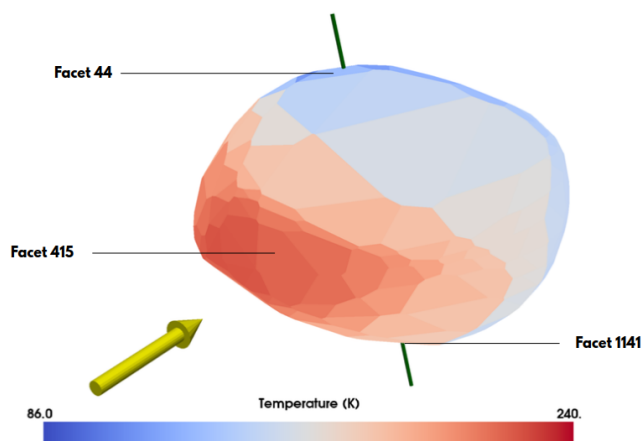


**Figure 47.** Surface temperature map predicted by TEMPEST for a thermal inertia of  $40 \text{ J m}^{-2} \text{ K}^{-1} \text{ s}^{-1/2}$ , at a heliocentric distance corresponding to the semi-major axis of 2.6 au. Facets 44, 415, and 1141 on the surface represent the north pole, equator, and south pole, respectively.

variations show strong dependence on both latitude and longitude, owing to Justitia's irregular shape and pole orientation/obliquity. For a nominal thermal inertia of  $40 \text{ J m}^{-2} \text{ K}^{-1} \text{ s}^{-1/2}$ , equatorial temperatures range from approximately 240 K near local noon to about 112 K on the night side during one rotation. The north pole reaches a maximum of  $\sim 136 \text{ K}$  and a minimum of  $\sim 87 \text{ K}$ , while the south pole reaches  $\sim 180 \text{ K}$  with a pre-dawn temperature of  $\sim 102 \text{ K}$ . Considering a thermal inertia of  $100 \text{ J m}^{-2} \text{ K}^{-1} \text{ s}^{-1/2}$ , equatorial temperatures range from  $\sim 235 \text{ K}$  to  $\sim 134 \text{ K}$  over one orbit, with the north

pole varying between  $\sim 125 \text{ K}$  and  $\sim 97 \text{ K}$ , and the south pole between  $\sim 170 \text{ K}$  and  $\sim 118 \text{ K}$ . Increasing thermal inertia to  $200 \text{ J m}^{-2} \text{ K}^{-1} \text{ s}^{-1/2}$ , equatorial temperatures vary from  $\sim 225 \text{ K}$  to  $\sim 150 \text{ K}$ , with the north pole ranging between  $\sim 118 \text{ K}$  and  $\sim 100 \text{ K}$ , and the south pole between  $\sim 160 \text{ K}$  and  $\sim 128 \text{ K}$ , reducing the amplitude by roughly 50% on the equator in comparison to  $\Gamma = 40$ .

Furthermore, regarding the overall temperature variation, our results show a difference of  $54 \text{ K}$  in relation to the minimum temperature and  $10 \text{ K}$  in relation to the maximum temperature when compared with the results of Hayne et al. (2024)

Figure 48 presents the predicted diurnal surface temperatures for different thermal inertia values at three representative surface regions (equator, north pole, and south pole), corresponding to those shown in Figure 47. Table 10 reports the surface temperatures for different heliocentric distances, considering perihelion and aphelion values. In the perihelion, we find day-side temperatures reaching  $\sim 275 \text{ K}$  near local noon and night-side minima of  $\sim 118 \text{ K}$ , corresponding to a median diurnal amplitude of  $\sim 157 \text{ K}$  at the equator. On the other hand, at aphelion, temperatures reach  $\sim 217 \text{ K}$  and drop to  $\sim 108 \text{ K}$  on the night side. All simulations indicate that the South Pole receives more insolation than the North Pole, as evidenced by its higher surface temperatures. Therefore, biogenic/primitive materials could be found better preserved at the North Pole. Thermal emission derived from these models can be used to generate synthetic thermal phase curves based on possible thermal inertia scenarios, which may serve in future work for di-

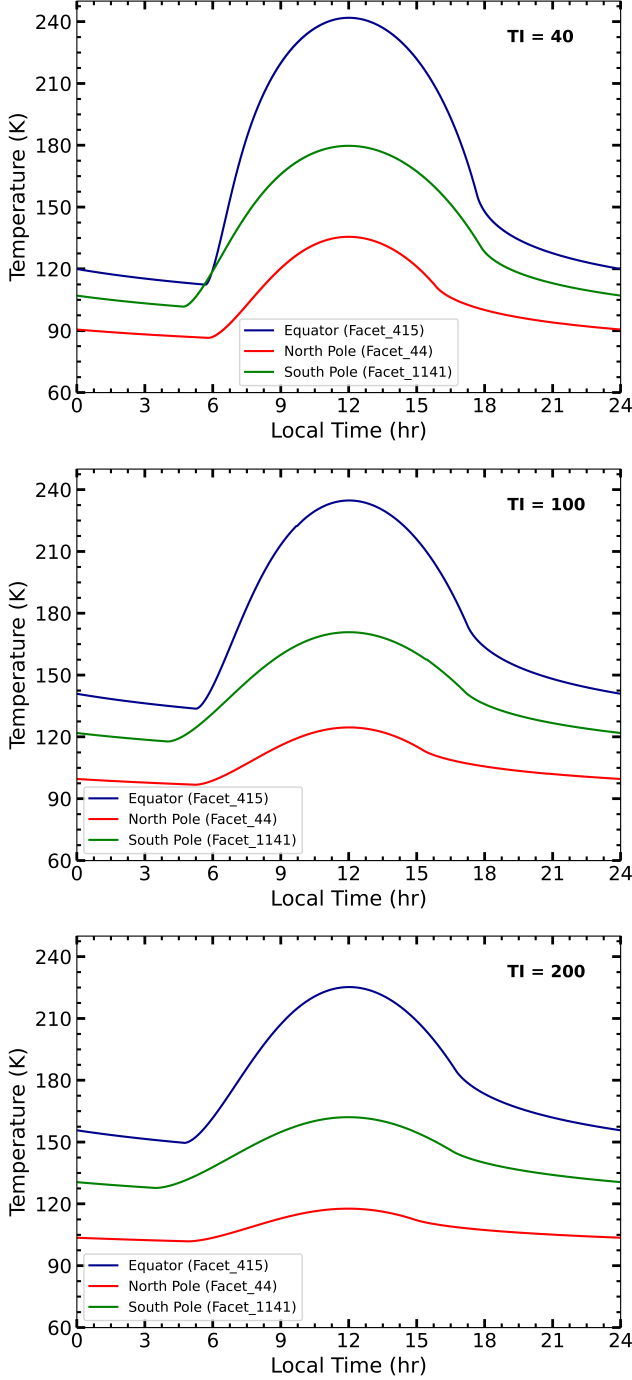


**Figure 48.** Predicted diurnal surface temperatures at three representative surface points corresponding to those shown in Fig. xx. Each plot is derived based on thermal inertia values of 40, 100, and 200  $\text{J m}^{-2} \text{K}^{-1} \text{s}^{-1/2}$ .

rect comparison with IR-cam and other instruments on the EMA payload.

**Table 8.** Physical and Thermal Properties of the Object

Parameter	Value	Units
$\lambda$	$73 \pm 11^a$	deg
$\beta$	$-81 \pm 15^a$	deg
Albedo	$0.06^a$	–
Emissivity	$0.9^a$	–
Thermal inertia	$41^a$	$\text{J m}^{-2} \text{K}^{-1} \text{s}^{-1/2}$
Solar distance (Main-Belt)	$2.06\text{--}3.17^d$	au
Rotational period	$33.12962^a$	h
Density	$1000^b$	$\text{kg m}^{-3}$
Specific heat capacity	$750^c$	$\text{J kg}^{-1} \text{K}^{-1}$

<sup>a</sup>Marciniak et al. (2025)

<sup>b</sup>(Buie et al. 2025)

<sup>c</sup>(Piqueux et al. 2021)

<sup>d</sup>JPL Small-Body Database: <https://ssd.jpl.nasa.gov/>.

## 15. CONCLUSION

In this work, we present for the first time a detailed analysis of the surface and orbital dynamics of asteroid (269) Justitia, a member of the main asteroid belt with an unusual characteristic: it is an ultra-red (Z-type) asteroid. We use its 3-D polyhedral shape model and its equivalent ellipsoidal model to analyze the surface dynamics and planar symmetric periodic orbits around it.

The analysis of the geopotential and surface acceleration showed that the gravitational potential dominates the dynamical environment around asteroid Justitia, a consequence of its slow rotation. We also show that the global behavior of the geopotential and surface acceleration of Justitia remains unchanged for densities from  $1.0 \text{ g cm}^{-3}$  to  $2.0 \text{ g cm}^{-3}$ .

We also identified that the variation in its tilts does not exceed  $50^\circ$ . We found that 97.5% of Justitia’s surface has slopes below  $40^\circ$ . Regarding its escape speed, it exhibits typical behavior for slowly rotating small bodies: the regions of maximum escape speed correspond to the regions with the minimum geopotential.

Furthermore, we analyzed the gravitational effects of Solar Radiation Pressure at the apocenter and pericenter of its current orbit, and also considering it in the past in the Kuiper belt at  $\sim 40$  au. The data obtained indicate that particles on the surface of Justitia larger than  $1 \mu\text{m}$  at the pericentre,  $3 \times 10^{-1} \mu\text{m}$  at the apocentre, and  $5.0 \times 10^{-3}$  in the past, at  $\sim 40$  au, are negligibly affected by solar radiation pressure. We also analyzed the effects of third-body perturbation on Justitia’s slopes, and our results indicate that this perturbation has a negligible influence on the overall behavior of the slopes.

Investigation of the zero-velocity curves in projection planes  $xOy$ ,  $xOz$ , and  $yOz$  confirms the existence

of the five equilibrium points about asteroid Justitia, regarding the densities from  $1.0\text{ g cm}^{-3}$  to  $2.0\text{ g cm}^{-3}$  and a rotational period of and a rotational period of 33.12962 h. Regarding the topological structure of equilibrium points at the xOy plane, our results show that equilibrium points  $E_1$  and  $E_3$  are unstable. Equilibrium points  $E_2$ ,  $E_4$ , and  $E_5$  are linearly stable, with  $E_5$  located internally to the asteroid. We also observed that as the density increases, the gravitational pull becomes stronger. This result is also consistent, as we analyzed the evolution of equilibrium points, assuming that Justitia had a faster spin in the past. Consequently, the external equilibrium points shift outward, while the internal equilibrium point shifts inward to the Justitia center of mass. The equilibrium point  $E_3$  has the minimum geopotential.

The results about return speed show that the regions of maximum and minimum return speed correspond to the areas of maximum and minimum escape speed, respectively.

We also identified 28 new families of planar-symmetric periodic orbits around Justitia, using an equivalent ellipsoidal shape model for this purpose, expanded in a series of spherical harmonics up to fourth order. We analyzed the orbits of these families and their orbital stability. For a space mission, the ideal scenario is one of orbital stability ( $K < 2$ ) or low values of  $K > 2$ , as the orbit can still be utilized in specific, controlled orbital strategies.

Finally, we believe that our results could guide future investigations of the Emirates Mission to the Asteroid Belt (EMA) about the dynamic environment of the ultra-red asteroid (269) Justitia. Our analyses could also be applied to other similar small bodies in the Solar System that rotate slowly.

Our results have broader implications: the reliable constraints on the surface dynamics and orbital environment of Justitia, together with the knowledge of possible trajectories, will facilitate mission planning for the MBR Explorer, including in situ operations and landing strategies. In addition, we present thermal modeling results for Justitia at different thermal inertia values and heliocentric distances, along with detailed temperature maps of the asteroid. These results provide informa-

tion on the surface temperatures and highlight which regions receive more insolation, thereby indicating the colder areas of the object where materials may be better preserved. We found that the south pole receives more insolation than the north pole, with minimum temperatures of 102 K and 87 K, respectively. Consequently, the quality of data obtained during the mission, when compared with pre-mission predictions, will provide crucial ground truth for asteroid studies based on remote sensing and ground-based methods.

## ACKNOWLEDGMENTS

A. Amarante and A. Ferreira thank the financial support of the São Paulo Research Foundation (FAPESP) [grants #2023/11781-5 & #2025/15438-9]. FM thanks the financial support from the São Paulo Research Foundation (FAPESP), Brazil, under Process Number 2024/16260-6. The authors also acknowledge the financial support of the Coordination for the Improvement of Higher Education Personnel (CAPES) - Brazil (finance code 001). This research was also supported by computational resources supplied by the Center for Scientific Computing (NCC/GridUNESP) of the São Paulo State University (UNESP) and the Center for Mathematical Sciences Applied to Industry (CeMEAI), funded by FAPESP [grant #2013/07375-0].

## DATA AVAILABILITY

**Data availability** The dataset generated in this work is publicly available on Zenodo at <https://doi.org/10.5281/zenodo.18327490>.

**Code availability** The numerical codes used in this work can be found at GitHub: <https://github.com/amarante>

**Conflict of interest** The authors declare no conflict of interest.

## AUTHOR CONTRIBUTIONS

LB, AA, AF, FM, and MM equally contributed to this work. LB, AA, AF, FM, and MM performed numerical simulations, figures, and wrote the manuscript. AA, AF, and FM revised the manuscript.

## APPENDIX

### A. COMPUTATION OF GRAVITATIONAL FIELD

The analytical expressions for the gravitational potential, the gravitational attraction vector, and the gravitational gradient matrix, with singularity corrections, can be written as follows for a homogeneous asteroid of constant density

$\rho$  (Tsoulis & Petrovi 2001).

$$U(x_1, x_2, x_3) = -\frac{G\rho}{2} \sum_{p=1}^n \sigma_p h_p \left[ \sum_{q=1}^m \sigma_{pq} h_{pq} L_{N_{pq}} + h_p \sum_{q=1}^m \sigma_{pq} A_{N_{pq}} + \sin(gA_p) \right], \quad (\text{A1})$$

$$-\frac{\partial U(x_1, x_2, x_3)}{\partial x_i} = -G\rho \sum_{p=1}^n \cos(\mathbf{N}_p, \mathbf{e}_i) \left[ \sum_{q=1}^m \sigma_{pq} h_{pq} L_{N_{pq}} + h_p \sum_{q=1}^m \sigma_{pq} A_{N_{pq}} + \sin(gA_p) \right], \quad (\text{A2})$$

$(i = 1, 2, 3),$

$$-\frac{\partial^2 U(x_1, x_2, x_3)}{\partial x_i \partial x_j} = G\rho \sum_{p=1}^n \cos(\mathbf{N}_p, \mathbf{e}_i) \left[ \sum_{q=1}^m \cos(\mathbf{n}_{pq}, \mathbf{e}_j) L_{N_{pq}} + \sigma_p \cos(\mathbf{N}_p, \mathbf{e}_j) \sum_{q=1}^m \sigma_{pq} A_{N_{pq}} + \sin(gB_{pj}) \right], \quad (i, j = 1, 2, 3). \quad (\text{A3})$$

Auxiliary functions are defined by:

$$L_{N_{pq}} = \ln \left( \frac{s_{2pq} + l_{2pq}}{s_{1pq} + l_{1pq}} \right), \quad (\text{A4})$$

$$A_{N_{pq}} = \arctan \left( \frac{h_p s_{2pq}}{h_{pq} l_{2pq}} \right) - \arctan \left( \frac{h_p s_{1pq}}{h_{pq} l_{1pq}} \right). \quad (\text{A5})$$

The variables  $x_1, x_2, x_3$  represent the coordinates of the test point in the reference system. The polyhedral model is homogeneous, with constant density  $\rho = M/V$ , and its shape is composed of  $n$  faces, each containing  $m$  edges. The gravitational constant is  $G = 6,67408 \times 10^{-20} \text{ km}^3 \text{ kg}^{-1} \text{ s}^{-2}$ . Each face defines a polygonal plane  $S_p$ , whose unit normal is the vector  $\mathbf{N}_p$ . The orthogonal projection of the point  $P(x_1, x_2, x_3)$  onto the plane of the face is denoted by  $P'$ , and the projection of  $P'$  onto the edge  $G_{pq}$ , belonging to the face  $S_p$ , is called  $P''$ . The distance between  $P$  and the plane of the face is  $h_p$ , while the distance between  $P'$  and  $P''$  is  $h_{pq}$ . The vectors  $\mathbf{e}_i$  and  $\mathbf{e}_j$  are the unit vectors of the geographic missions. The vector  $\mathbf{n}_{pq}$  is a unit vector contained in the plane of the face, perpendicular to the edge  $G_{pq}$ , and is oriented outwards from the polyhedron. The sign  $\sigma_{pq}$  assumes the value  $-1$  when  $\mathbf{n}_{pq}$  points to the half-plane containing  $P'$ , and  $+1$  otherwise.

The distances  $l_{1pq}$  and  $l_{2pq}$  are the distances between the point  $P$  and the two endpoints of the edge  $G_{pq}$ , while  $s_{1pq}$  and  $s_{2pq}$  are the distances between  $P''$  and these same endpoints. The terms  $\cos(\mathbf{N}_p, \mathbf{e}_i)$  and  $\cos(\mathbf{n}_{pq}, \mathbf{e}_j)$  are the directed cosines between the normal and common vectors. Finally, the terms  $\sin(gA_p)$  and  $\sin(gB_{pj})$  involve the singularity corrections that arise when the point  $P$  is exactly on the face, on an edge, or at a vertex of the polyhedron. These terms are zero when the point is outside the projection of the corresponding face.

## B. EIGENVALUES

**Table 9.** Eigenvalues ( $\lambda_n \times 10^{-5}$ ,  $n = 1, 2, \dots, 6$ ) corresponding to the equilibrium points in the Justitia gravitational field, calculated for different density values and a rotational period of 33.12962 h; utilizing MINOR-EQUILIBRIA package (Amarante & Winter 2020).

Point	Density ( $\text{g cm}^{-3}$ )	$\lambda_{1,2}$	$\lambda_{3,4}$	$\lambda_{5,6}$	Topological Structure
E <sub>1</sub>	1.0	$\pm 0.863$	$\pm 5.325i$	$\pm 5.282i$	saddle-centre-centre
	1.2	$\pm 0.809$	$\pm 5.318i$	$\pm 5.280i$	
	1.4	$\pm 0.813$	$\pm 5.313i$	$\pm 5.279i$	
	1.6	$\pm 0.832$	$\pm 5.309i$	$\pm 5.278i$	
	1.8	$\pm 0.831$	$\pm 5.306i$	$\pm 5.278i$	
	2.0	$\pm 0.831$	$\pm 5.304i$	$\pm 5.277i$	
E <sub>2</sub>	1.0	$\pm 0.831i$	$\pm 5.165i$	$\pm 5.305i$	centre-centre-centre
	1.2	$\pm 0.783i$	$\pm 5.177i$	$\pm 5.300i$	
	1.4	$\pm 0.793i$	$\pm 5.186i$	$\pm 5.292i$	
	1.6	$\pm 0.713i$	$\pm 5.193i$	$\pm 5.295i$	
	1.8	$\pm 0.686i$	$\pm 5.199i$	$\pm 5.198i$	
	2.0	$\pm 0.678i$	$\pm 5.205i$	$\pm 5.277i$	
E <sub>3</sub>	1.0	$\pm 0.892$	$\pm 5.328i$	$\pm 5.305i$	saddle-centre-centre
	1.2	$\pm 0.835$	$\pm 5.321i$	$\pm 5.281i$	
	1.4	$\pm 0.831$	$\pm 5.316i$	$\pm 5.280i$	
	1.6	$\pm 0.832$	$\pm 5.312i$	$\pm 5.278i$	
	1.8	$\pm 0.823$	$\pm 5.309i$	$\pm 5.278i$	
	2.0	$\pm 0.831$	$\pm 5.306i$	$\pm 5.277i$	
E <sub>4</sub>	1.0	$\pm 0.840i$	$\pm 5.301i$	$\pm 5.168i$	centre-centre-centre
	1.2	$\pm 0.791i$	$\pm 5.297i$	$\pm 5.179i$	
	1.4	$\pm 0.752i$	$\pm 5.188i$	$\pm 5.188i$	
	1.6	$\pm 0.720i$	$\pm 5.195i$	$\pm 5.194i$	
	1.8	$\pm 0.693i$	$\pm 5.200i$	$\pm 5.206i$	
	2.0	$\pm 0.669i$	$\pm 5.205i$	$\pm 5.207i$	
E <sub>5</sub>	1.0	$\pm 59.278i$	$\pm 54.893i$	$\pm 43.767i$	centre-centre-centre
	1.2	$\pm 64.933i$	$\pm 59.662i$	$\pm 48.417i$	
	1.4	$\pm 70.134i$	$\pm 64.052i$	$\pm 52.689i$	
	1.6	$\pm 74.975i$	$\pm 68.140i$	$\pm 56.663i$	
	1.8	$\pm 79.521i$	$\pm 71.983i$	$\pm 60.392i$	
	2.0	$\pm 83.822i$	$\pm 75.620i$	$\pm 63.916i$	

### C. TEMPERATURES IN DIFFERENT REGIONS

**Table 10.** Maximum and minimum temperatures of the three different regions/facets for different thermal inertia values and solar distances.

Facet	Distance 2.6 au (K)	Distance 2.05 au (K)	Distance 3.18 au (K)
Thermal Inertia = 40 J m <sup>-2</sup> K <sup>-1</sup> s <sup>-1/2</sup>			
Facet_415 (Equator)	Max: 241.85	Max: 274.09	Max: 217.11
	Min: 112.34	Min: 117.59	Min: 107.85
Facet_44 (North Pole)	Max: 135.55	Max: 156.78	Max: 119.37
	Min: 86.52	Min: 92.09	Min: 81.63
Facet_1141 (South Pole)	Max: 179.71	Max: 204.87	Max: 160.31
	Min: 101.67	Min: 107.20	Min: 96.89
Thermal Inertia = 100 J m <sup>-2</sup> K <sup>-1</sup> s <sup>-1/2</sup>			
Facet_415 (Equator)	Max: 234.72	Max: 268.18	Max: 208.87
	Min: 133.68	Min: 141.01	Min: 127.27
Facet_44 (North Pole)	Max: 124.57	Max: 145.12	Max: 109.65
	Min: 96.78	Min: 104.98	Min: 89.76
Facet_1141 (South Pole)	Max: 170.79	Max: 196.89	Max: 151.01
	Min: 117.75	Min: 125.82	Min: 110.72
Thermal Inertia = 200 J m <sup>-2</sup> K <sup>-1</sup> s <sup>-1/2</sup>			
Facet_415 (Equator)	Max: 225.22	Max: 259.71	Max: 198.94
	Min: 149.59	Min: 159.38	Min: 140.98
Facet_44 (North Pole)	Max: 117.67	Max: 136.16	Max: 104.42
	Min: 101.81	Min: 112.05	Min: 93.44
Facet_1141 (South Pole)	Max: 162.06	Max: 187.61	Max: 143.32
	Min: 127.73	Min: 138.50	Min: 118.58

## REFERENCES

- Abad, A., Arribas, M., Palacios, M., & Elife, A. 2023, Evolution of the characteristic curves in the restricted three-body problem in terms of the mass parameter, *Celestial Mechanics and Dynamical Astronomy*, 135, 7
- Almazmi, H., Hayne, P., Landis, M., & Bottke, W. 2024, Science Overview of the Emirates Mission to the Asteroid Belt, 45th COSPAR Scientific Assembly. Held 13-21 July, 45, 261
- AlSaeed, N., AlMazmi, H., & Hayne, P. 2025, in EPSC-DPS Joint Meeting 2025 (EPSC-DPS2025, EPSC-DPS2025-1435, doi: [10.5194/epsc-dps2025-1435](https://doi.org/10.5194/epsc-dps2025-1435))
- Amarante, A. 2020a, Minor-Gravity Package, v2.1, Zenodo, doi: [10.5281/zenodo.4043553](https://doi.org/10.5281/zenodo.4043553)
- . 2020b, Minor-Equilibria-NR Package, v1.2, Zenodo, doi: [10.5281/zenodo.4043461](https://doi.org/10.5281/zenodo.4043461)
- Amarante, A., & Winter, O. C. 2020, Surface dynamics, equilibrium points and individual lobes of the Kuiper Belt object (486958) Arrokoth, *MNRAS*, 496, 4154, doi: [10.1093/mnras/staa1732](https://doi.org/10.1093/mnras/staa1732)
- Amarante, A., & Winter, O. C. 2022, The fate of particles in the dynamical environment around Kuiper-Belt object (486958) Arrokoth, *Astrophysics and Space Science*, 367, 38, doi: [10.1007/s10509-022-04065-2](https://doi.org/10.1007/s10509-022-04065-2)
- Amarante, A., Winter, O. C., & Sfair, R. 2021, Stability and Evolution of Fallen Particles Around the Surface of Asteroid (101955) Bennu, *Journal of Geophysical Research (Planets)*, 126, e06272, doi: [10.1029/2019JE006272](https://doi.org/10.1029/2019JE006272)
- Barrio, R., & Blesa, F. 2009, Systematic search of symmetric periodic orbits in 2DOF Hamiltonian systems, *Chaos, Solitons & Fractals*, 41, 560
- Braga, L., Amarante, A., Ferreira, A., Gomes, C., & Ceranto, L. 2025, Equilibrium points and surface dynamics about comet 67P/Churyumov-Gerasimenko, *European Physical Journal Special Topics*, doi: [10.1140/epjs/s11734-025-01986-1](https://doi.org/10.1140/epjs/s11734-025-01986-1)
- Brent, R. P. 1971, An algorithm with guaranteed convergence for finding a zero of a function, *The computer journal*, 14, 422
- Broucke, R., & Elife, A. 2005, The Dynamics of Orbits in a Potential Field of a Solid Circular Ring, *Pre-publicaciones del Seminario Matemático "García de Galdeano"*, N<sup>o</sup>. 7, 2005, 10, doi: [10.1070/RD2005v010n02ABEH000307](https://doi.org/10.1070/RD2005v010n02ABEH000307)
- Buie, M., Hayne, P., et al. 2025, Occultation-based Size and Shape of (269) Justitia, *The Planetary Science Journal*, 6, 61, doi: [10.3847/PSJ/adb28c](https://doi.org/10.3847/PSJ/adb28c)

- Burns, J. A., Lamy, P. L., & Soter, S. 1979, Radiation forces on small particles in the solar system, *Icarus*, 40, 1
- Deprit, A., & Henrard, J. 1967, Natural families of periodic orbits, *Astronomical Journal*, Vol. 72, p. 158 (1967), 72, 158
- Dobrovolskis, A. R. 1996, Inertia of Any Polyhedron, *Icarus*, 124, 698, doi: <https://doi.org/10.1006/icar.1996.0243>
- El-Maarry, M. R., Ivanov, A., Ansari, M. T., et al. 2025, The Lander of the Emirates Mission to explore the Asteroid Belt: Preliminary Design and Scientific Objectives, EPSC-DPS Joint Meeting 2025, doi: [10.5194/epsc-dps2025-1762](https://doi.org/10.5194/epsc-dps2025-1762)
- Elkins-Tanton, L. T., Asphaug, E., Bell, J. F., et al. 2017, in 48th Annual Lunar and Planetary Science Conference, Lunar and Planetary Science Conference, 1718
- Fu, X., Soldini, S., Ikeda, H., et al. 2024, The dynamics about asteroid (162173) Ryugu, *Celestial Mechanics and Dynamical Astronomy*, 136, 29, doi: [10.1007/s10569-024-10199-y](https://doi.org/10.1007/s10569-024-10199-y)
- Glassmeier, K.-H., Boehnhardt, H., Koschny, D., et al. 2007, The Rosetta Mission: Flying Towards the Origin of the Solar System, *SSRv*, 128, 1, doi: [10.1007/s11214-006-9140-8](https://doi.org/10.1007/s11214-006-9140-8)
- Hanuš, J., Delbo', M., Ďurech, J., & Alí-Lagoa, V. 2015, Thermophysical modeling of asteroids from WISE thermal infrared data - Significance of the shape model and the pole orientation uncertainties, *Icarus*, 256, 101, doi: [10.1016/j.icarus.2015.04.014](https://doi.org/10.1016/j.icarus.2015.04.014)
- Harish, Hayne, P. O., Emery, J. P., et al. 2025, Surface Composition of Asteroid 269 Justitia: Insights from Spectral Mixture Modeling, *The Astrophysical Journal*, 992, 125, doi: [10.3847/1538-4357/adff70](https://doi.org/10.3847/1538-4357/adff70)
- Harish, Hayne, P. O., Emery, J. P., et al. 2025, Surface Composition of Asteroid 269 Justitia: Insights from Spectral Mixture Modeling, *ApJ*, 992, 125, doi: [10.3847/1538-4357/adff70](https://doi.org/10.3847/1538-4357/adff70)
- Hasegawa, S., Marsset, M., DeMeo, F. E., et al. 2021, Discovery of Two TNO-like Bodies in the Asteroid Belt, *ApJL*, 916, L6, doi: [10.3847/2041-8213/ac0f05](https://doi.org/10.3847/2041-8213/ac0f05)
- Hayne, P. O., AlMazmi, H. A., Sorli, K., et al. 2024, in AGU Fall Meeting Abstracts, Vol. 2024, AGU Fall Meeting Abstracts, P21E-3024
- Hirabayashi, M., Mimasu, Y., Sakatani, N., et al. 2021, Hayabusa2 extended mission: New voyage to rendezvous with a small asteroid rotating with a short period, *Advances in Space Research*, 68, 1533, doi: [10.1016/j.asr.2021.03.030](https://doi.org/10.1016/j.asr.2021.03.030)
- Horányi, M. 1996, Unusual dynamics of circumplanetary dust, *ASP Conference Series (Completing the Inventory of the Solar System)*, 107, 129
- Humes, O. A., Thomas, C. A., & McGraw, L. E. 2024, The Distribution of Highly Red-sloped Asteroids in the Middle and Outer Main Belt, *PSJ*, 5, 80, doi: [10.3847/PSJ/ad2e99](https://doi.org/10.3847/PSJ/ad2e99)
- Izidoro, A., de Souza Torres, K., Winter, O. C., & Haghighipour, N. 2013, A Compound Model for the Origin of Earth's Water, *ApJ*, 767, 54, doi: [10.1088/0004-637X/767/1/54](https://doi.org/10.1088/0004-637X/767/1/54)
- Jiang, Y. 2015, Equilibrium Points and Periodic Orbits in the Vicinity of Asteroids with an Application to 216 Kleopatra, *Earth Moon and Planets*, 115, 31, doi: [10.1007/s11038-015-9464-z](https://doi.org/10.1007/s11038-015-9464-z)
- Jiang, Y., & Baoyin, H. 2014, Orbital Mechanics near a Rotating Asteroid, *Journal of Astrophysics and Astronomy*, 35, 17, doi: [10.1007/s12036-014-9259-z](https://doi.org/10.1007/s12036-014-9259-z)
- Kaasalainen, M., & Torppa, J. 2001, Optimization Methods for Asteroid Lightcurve Inversion. I. Shape Determination, *Icarus*, 153, 24, doi: [10.1006/icar.2001.6673](https://doi.org/10.1006/icar.2001.6673)
- Kaasalainen, M., Torppa, J., & Muinonen, K. 2001, Optimization Methods for Asteroid Lightcurve Inversion. II. The Complete Inverse Problem, *Icarus*, 153, 37, doi: [10.1006/icar.2001.6674](https://doi.org/10.1006/icar.2001.6674)
- Lara, M., Deprit, A., & Elipe, A. 1995, Numerical continuation of families of frozen orbits in the zonal problem of artificial satellite theory, *Celestial Mechanics and Dynamical Astronomy*, 62, 167
- Lauretta, D. S., Balram-Knutson, S. S., Beshore, E., & others. 2017, OSIRIS-REx: Sample Return from Asteroid (101955) Bennu, *SSRv*, 212, 925, doi: [10.1007/s11214-017-0405-1](https://doi.org/10.1007/s11214-017-0405-1)
- Lauretta, D. S., Dellagiustina, D. N., Bennett, C. A., et al. 2019, The unexpected surface of asteroid (101955) Bennu, *Nature*, 568, 55, doi: [10.1038/s41586-019-1033-6](https://doi.org/10.1038/s41586-019-1033-6)
- Levison, H. F., Marchi, S., Noll, K. S., Spencer, J. R., et al. 2024, A contact binary satellite of the asteroid (152830) Dinkinesh, *Nature*, 629, 1015, doi: [10.1038/s41586-024-07378-0](https://doi.org/10.1038/s41586-024-07378-0)
- Lewis, J. S. 1997, Book Review: Mining the sky : untold riches from the asteroids, comets, and planets / Addison-Wesley, 1996, *Astronomy*, 25, 104
- Lyster, D., Howett, C., & Penn, J. 2024, in European Planetary Science Congress, EPSC2024-1121, doi: [10.5194/epsc2024-1121](https://doi.org/10.5194/epsc2024-1121)
- Lyster, D., Howett, C., & Penn, J. 2025, in EPSC-DPS Joint Meeting 2025, Helsinki, Finland, 7-12 Sep 2025, EPSC-DPS2025-1479, doi: [10.5194/epsc-dps2025-1479](https://doi.org/10.5194/epsc-dps2025-1479)

- Mahlke, M., Carry, B., & Mattei, P. A. 2022, Asteroid taxonomy from cluster analysis of spectrometry and albedo, *A&A*, 665, A26, doi: [10.1051/0004-6361/202243587](https://doi.org/10.1051/0004-6361/202243587)
- Marchi, S., Vokrouhlický, D., Nesvorný, D., Bottke, W. F., & others. 2025, A Pre-flyby View on the Origin of Asteroid Donaldjohanson, a Target of the NASA Lucy Mission, *PSJ*, 6, 59, doi: [10.3847/PSJ/adb4f4](https://doi.org/10.3847/PSJ/adb4f4)
- Marchis, F., Durech, J., Castillo-Rogez, J., Vachier, F., et al. 2014, The Puzzling Mutual Orbit of the Binary Trojan Asteroid (624) Hektor, *ApJL*, 783, L37, doi: [10.1088/2041-8205/783/2/L37](https://doi.org/10.1088/2041-8205/783/2/L37)
- Marciniak, A., Choukroun, A., Perła, J., & others. 2025, Thermophysical Model of (269) Justitia—Main Belt Asteroid Possibly Implanted from Trans-Neptunian Region, *The Planetary Science Journal*, 6, 60, doi: [10.3847/PSJ/adb28b](https://doi.org/10.3847/PSJ/adb28b)
- Markellos, V., Black, W., & Moran, P. 1974, A grid search for families of periodic orbits in the restricted problem of three bodies, *Celestial mechanics*, 9, 507
- McMahon, J. W., Scheeres, D. J., Baker, D., et al. 2023, in *LPI Contributions*, Vol. 2851, Asteroids, Comets, Meteors Conference, 2296
- Mignard, F. 1982, Radiation pressure and dust particle dynamics, *Icarus*, 49, 347, doi: [https://doi.org/10.1016/0019-1035\(82\)90041-0](https://doi.org/10.1016/0019-1035(82)90041-0)
- Mignard, F. 1984, Effects of radiation forces on dust particles in planetary rings, *IAU Colloq. 75: Planetary Rings*, 333
- Morbidelli, A. 2010, A coherent and comprehensive model of the evolution of the outer Solar System, *Comptes Rendus. Physique*, 11, 651–659, doi: [10.1016/j.crhy.2010.11.001](https://doi.org/10.1016/j.crhy.2010.11.001)
- Morbidelli, A., Chambers, J., Lunine, J. I., et al. 2000, Source regions and time scales for the delivery of water to Earth, *M&PS*, 35, 1309, doi: [10.1111/j.1945-5100.2000.tb01518.x](https://doi.org/10.1111/j.1945-5100.2000.tb01518.x)
- Morbidelli, A., Levison, H. F., Tsiganis, K., & Gomes, R. 2005, Chaotic capture of Jupiter’s Trojan asteroids in the early Solar System, *Nature*, 435, 462, doi: [10.1038/nature03540](https://doi.org/10.1038/nature03540)
- Moura, T. S., Winter, O. C., Amarante, A., et al. 2020, Dynamical environment and surface characteristics of asteroid (16) Psyche, *MNRAS*, 491, 3120, doi: [10.1093/mnras/stz3210](https://doi.org/10.1093/mnras/stz3210)
- Mueller, M., Marchis, F., Emery, J. P., et al. 2010, Eclipsing binary Trojan asteroid Patroclus: Thermal inertia from Spitzer observations, *Icarus*, 205, 505, doi: [10.1016/j.icarus.2009.07.043](https://doi.org/10.1016/j.icarus.2009.07.043)
- Murray, C. D., & Dermott, S. F. 1999, *Solar System Dynamics* (Cambridge University Press), doi: [10.1017/CBO9781139174817](https://doi.org/10.1017/CBO9781139174817)
- Parker, J., Hameli, F., Knittel, J., et al. 2024, in *ConferencePaper*, 1–22
- Parker, J. S., & Anderson, R. L. 2014, *Low-energy lunar trajectory design* (John Wiley & Sons)
- Pilcher, F. 2016, Rotation Period Determination for 269 Justitia, 275 Sapiientia 331 Etheridgea, and 609 Fulvia, *Minor Planet Bulletin*, 43, 135
- Piqueux, S., Vu, T. H., Bapst, J., et al. 2021, Specific Heat Capacity Measurements of Selected Meteorites for Planetary Surface Temperature Modeling, *Journal of Geophysical Research (Planets)*, 126, e07003, doi: [10.1029/2021JE007003](https://doi.org/10.1029/2021JE007003)
- Riaguas, A., Elipe, A., & Lara, M. 1999, Periodic Orbits Around a Massive Straight Segment, *Celestial Mechanics and Dynamical Astronomy*, 73, 169, doi: [10.1023/A:1008399030624](https://doi.org/10.1023/A:1008399030624)
- Riaguas, A., Elipe, A., & López-Moratalla, T. 2001, Non-linear stability of the equilibria in the gravity field of a finite straight segment, *Celestial Mechanics and Dynamical Astronomy*, 81, 235
- Roll, R., Witte, L., & Arnold, W. 2016, ROSETTA lander Philae - soil strength analysis, *Icarus*, 280, 359, doi: [10.1016/j.icarus.2016.07.004](https://doi.org/10.1016/j.icarus.2016.07.004)
- Russell, R. P. 2006, Global search for planar and three-dimensional periodic orbits near Europa, *The Journal of the Astronautical Sciences*, 54, 199
- Scheeres, D. 2012, *Orbital Motion in Strongly Perturbed Environments, Orbital Motion in Strongly Perturbed Environments*, by Scheeres, Daniel J. ISBN: 978-3-642-03255-4. Berlin: Springer, 2012, doi: [10.1007/978-3-642-03256-1](https://doi.org/10.1007/978-3-642-03256-1)
- Scheeres, D., McMahon, J., Villa, J. Pugliatti, M., et al. 2025, Gravity Science Goals for the UAE EMA Mission, EGU General Assembly, doi: <https://doi.org/10.5194/egusphere-egu25-13874>
- Scheeres, D. J. 1994, Dynamics about Uniformly Rotating Triaxial Ellipsoids: Applications to Asteroids, *Icarus*, 110, 225, doi: [10.1006/icar.1994.1118](https://doi.org/10.1006/icar.1994.1118)
- Scheeres, D. J., Hesar, S. G., Tardivel, S., et al. 2016, The geophysical environment of Bennu, *Icarus*, 276, 116, doi: [10.1016/j.icarus.2016.04.013](https://doi.org/10.1016/j.icarus.2016.04.013)
- Scheeres, D. J., Ostro, S. J., Hudson, R. S., DeJong, E. M., & Suzuki, S. 1998, Dynamics of Orbits Close to Asteroid 4179 Toutatis, *Icarus*, 132, 53, doi: [10.1006/icar.1997.5870](https://doi.org/10.1006/icar.1997.5870)

- Sorli, K., Hayne, P. O., AlMazmi, H. A., H, H., & Edwards, C. S. 2024, in AGU Fall Meeting Abstracts, Vol. 2024, P23G-07
- Spencer, J. R., Lebofsky, L. A., & Sykes, M. V. 1989, Systematic biases in radiometric diameter determinations, *Icarus*, 78, 337, doi: [10.1016/0019-1035\(89\)90182-6](https://doi.org/10.1016/0019-1035(89)90182-6)
- Stern, S. A. 2008, The New Horizons Pluto Kuiper Belt Mission: An Overview with Historical Context, *SSRv*, 140, 3, doi: [10.1007/s11214-007-9295-y](https://doi.org/10.1007/s11214-007-9295-y)
- Stern, S. A., Weaver, H. A., Spencer, J. R., et al. 2019, Initial results from the New Horizons exploration of 2014 MU 69 , a small Kuiper Belt object, *Science*, 364, aaw9771, doi: [10.1126/science.aaw9771](https://doi.org/10.1126/science.aaw9771)
- Tsiganis, K., Gomes, R., Morbidelli, A., & Levison, H. F. 2005, Origin of the orbital architecture of the giant planets of the Solar System, *Nature*, 435, 459, doi: [10.1038/nature03539](https://doi.org/10.1038/nature03539)
- Tsirogiannis, G., Perdios, E., & Markellos, V. 2009, Improved grid search method: An efficient tool for global computation of periodic orbits: Application to Hill's problem, *Celestial Mechanics and Dynamical Astronomy*, 103, 49
- Tsouliis, D. 2012, Analytical computation of the full gravity tensor of a homogeneous arbitrarily shaped polyhedral source using line integrals, *Geophysics*, 77, F1, doi: [10.1190/geo2010-0334.1](https://doi.org/10.1190/geo2010-0334.1)
- Tsouliis, D., & Petrovi, S. 2001, On the singularities of the gravity field of a homogeneous polyhedral body, *Geophysics*, 66, 535, doi: [10.1190/1.1444944](https://doi.org/10.1190/1.1444944)
- Werner, R. A. 1994, The Gravitational Potential of a Homogeneous Polyhedron or Don't Cut Corners, *Celestial Mechanics and Dynamical Astronomy*, 59, 253, doi: [10.1007/BF00692875](https://doi.org/10.1007/BF00692875)
- Werner, R. A. 1997, Spherical harmonic coefficients for the potential of a constant-density polyhedron, *Computers & Geosciences*, 23, 1071, doi: [https://doi.org/10.1016/S0098-3004\(97\)00110-6](https://doi.org/10.1016/S0098-3004(97)00110-6)
- Werner, R. A., & Scheeres, D. J. 1996, Exterior gravitation of a polyhedron derived and compared with harmonic and mascon gravitation representations of asteroid 4769 Castalia, *Celestial Mechanics and Dynamical Astronomy*, 65, 313, doi: [10.1007/BF00053511](https://doi.org/10.1007/BF00053511)
- Winter, O. C., Valvano, G., Moura, T. S., et al. 2020, Asteroid triple-system 2001 SN263: surface characteristics and dynamical environment, *Monthly Notices of the Royal Astronomical Society*, 492, 4437, doi: [10.1093/mnras/staa097](https://doi.org/10.1093/mnras/staa097)